The G1/S transition is promoted by Rb degradation via the E3 ligase UBR5

Shuyuan Zhang[1], Lucas Fuentes Valenzuela[1], Evgeny Zatulovskiy[1], Lise Mangiante[3], Christina Curtis[3], and Jan M. Skotheim[1,2,*]

[1]Department of Biology, Stanford University, Stanford, CA 94305
[2]Chan Zuckerberg Biohub, San Francisco, CA 94158
[3]Stanford Cancer Institute, Stanford, CA 94305
[*]Address correspondence to skotheim@stanford.edu

Summary

Mammalian cells make the decision to divide at the G1/S transition in response to diverse signals impinging on the retinoblastoma protein Rb, a cell cycle inhibitor and tumor suppressor. Rb is inhibited by two parallel pathways. In the canonical pathway, Cyclin D-Cdk4/6 kinase complexes phosphorylate and inactivate Rb. In the second, recently discovered pathway, Rb's concentration decreases during G1 to promote cells progressing through the G1/S transition. However, the mechanisms underlying this second pathway are unknown. Here, we found that Rb's concentration drop in G1 and recovery in S/G2 is controlled by phosphorylation-dependent protein degradation. In early G1 phase, un- and hypo-phosphorylated Rb is targeted by the E3 ligase UBR5. *UBR5* knockout cells have higher Rb concentrations in early G1, exhibit a lower G1/S transition rate, and are more sensitive to Cdk4/6 inhibition. This last observation suggests that UBR5 inhibition can strengthen the efficacy of Cdk4/6 inhibitor-based cancer therapies.

Key words: Retinoblastoma protein, protein degradation, ubiquitination, G1/S transition, E3 ubiquitin ligase, UBR5.

Introduction

The decision to divide often takes place in the G1 phase of the cell cycle and occurs in response to diverse input signals. Once taken, the decision to initiate DNA replication and divide is difficult to reverse despite changes to the input signals [1,2]. From a molecular point of view, the commitment point at the G1/S transition in response to growth signals corresponds to the hyper-phosphorylation and inactivation of the transcriptional inhibitor Rb, the retinoblastoma protein [1,3,4]. Hyper-phosphorylation of Rb frees the activating E2F transcription factors to drive expression of the Cyclin E and A, which can form complexes with the cyclin-dependent kinase Cdk2. Active Cyclin E/A-Cdk2 complexes then maintain Rb hyper-phosphorylation so that E2F-dependent transcription remains active throughout S phase [5]. While the molecular basis of the commitment point to cell division is increasingly well understood[1,2,6–8], we know much less about how the upstream input signals transmit quantitative information to the decision point.

Two distinct input pathways regulating the G1/S transition operate by inactivating Rb. The first pathway, which is the canonical pathway, acts through Cyclin-Cdk complexes phosphorylating Rb. Decades of work has gradually unveiled the molecular mechanisms underlying this pathway [5,9–12]. The upstream growth factors initiate signals that increase the expression of Cyclin D [13], which primarily forms a complex with the cyclin-dependent kinases Cdk4 and Cdk6 [14]. Cyclin D-Cdk4/6 complexes then initiate the phosphorylation of Rb, possibly through hypo- or mono-phosphorylation [15,16]. The hypo-phosphorylation of Rb likely shifts the dissociation constant (K_d) of Rb with E2F, thus promoting the G1/S transition. Once Rb is hyper-phosphorylated, possibly by the increasing Cyclin E-Cdk2 activity and the initial Cyclin D-Cdk4/6 activity, it is fully inactivated so that E2F can drive the E2F-dependent S phase transcription program. This Rb phosphorylation pathway is frequently hijacked in cancers to drive cell proliferation [17–21]. For example, Cyclin D amplification is a frequent mutation in breast cancer patients and is associated with shorter relapse free survival [17,22]. Moreover, increasing the Cyclin D-Cdk4 activity by transducing cells with a *CDK4* construct is a common approach to immortalize cells *in vitro* [23,24]. In fact, for many cancer cell lines and immortalized cell lines, Rb is immediately hyper-phosphorylated after cell birth due to a high Cdk activity likely arising both from mutations selected for proliferation and from the rich *in vitro* culture environment [2,25].

A second pathway that inactivates Rb, which we recently identified, operates through decreasing the concentration of the Rb protein during cell growth in G1 [26–28]. Specifically, the total amount of Rb protein stays relatively constant throughout G1, while the cell is growing bigger, so that its concentration decreases. In contrast, the concentrations of G1/S activators, including Cyclin D and E2F, stay constant during early to mid G1. These differential effects on protein concentration in G1 phase drive relative changes in the activities of the cell cycle inhibitor (Rb) and activators (E2F, Cyclin D) to favor progression through the G1/S transition.

Thus, our current model is that two Rb-inactivation pathways cooperate to activate E2F-dependent transcription and initiate the cell cycle[26–28] (Figure 1A). Namely, Cyclin D-dependent Rb hypo-phosphorylation shifts the dissociation constant (K_d) of Rb with E2F so that the decreasing Rb concentration can drop below K_d to release active E2F. Following the G1/S transition, Rb's concentration increases during S/G2/M to reset for the next cell cycle. Unlike the Cdk-dependent pathway, the Rb-dilution pathway does not depend on any increased Cdk activity and can serve as a parallel mechanism to inactivate Rb and promote the G1/S transition. Although several molecular mechanisms underlying Cyclin D synthesis and Rb phosphorylation have been elucidated [15,29], the molecular mechanism underlying the second pathway that decreases Rb concentration through G1 is unknown.

Here, we sought to determine the molecular mechanisms underlying Rb's concentration decrease through G1 (Figure 1A), an important signal triggering the G1/S transition. We found that Rb is consistently synthesized throughout the cell cycle, but its degradation is cell cycle dependent. Specifically, Rb is targeted for degradation in G1 by the E3 ligase UBR5 and stabilized by hyper-phosphorylation at the G1/S transition. A mathematical model shows that this mechanism is sufficient to explain the observed concentration dynamics through the cell cycle. Disruption of this Rb degradation mechanism via UBR5 deletion decreases the G1/S transition rate and sensitizes cells to chemical inhibition of Cdk4/6 activity. This last observation provides implications for improving the efficacy of Cdk4/6 inhibitor based therapies through targeting UBR5. Indeed, we observe frequent amplification of *UBR5* in breast cancer patients that is associated with worse prognosis.

Results

Rb concentration dynamics regulate cell cycle progression in cells born with low Cdk activity

While the decreasing Rb concentration in G1 drove cell cycle progression in some cells [26,27], many cell lines appeared to not respond to changes in Rb dosage in terms of their proliferation rate [16,30]. We therefore sought to further test the effect of Rb concentration on cell cycle progression and identify the reason behind this apparent discrepancy. To do this, we performed live-cell imaging on *HMEC-hTERT1* (telomerase-immortalized human mammary epithelial, abbreviated as HMEC) cells expressing endogenously tagged *RB1-3xFLAG-Clover-sfGFP* and the HDHB Cdk activity sensor [25]. The nuclear-to-cytoplasmic translocation of this fluorescent sensor marks the transition point in mid/late-G1 when Cdk activity abruptly increases (Figure 1B) [1,25]. Based on how quickly the Cdk activity rises after birth, we classified the cells into two categories: Cdk-high cells and Cdk-low cells based on whether or not Cdk activity had risen 5 hours after birth (Figure 1B, C; Figure S1C). This classification has been used in other studies that applied the same Cdk sensor on MCF10A cells [25]. When we aligned the cell traces to the inflection point of the HDHB sensor that marks Cdk activity increase, we found that the concentration of Rb continuously decreases during early- to mid-G1 phase in the Cdk-low cells, and then increases through the remainder of the cell cycle (Figure 1D; Figure S1A, B, D-G). However, Cdk-high cells do not exhibit decreasing Rb concentration dynamics in G1 (Figure 1D; Figure S1A, B, D-G). Thus, an Rb concentration decrease in G1 could only regulate the cell cycle in Cdk-low cells, but not in Cdk-high cells, where the concentration decrease does not take place and Rb is likely rapidly inactivated.

To test if the decrease in Rb concentration promotes cell cycle entry in Cdk-low cells, we examined the relationship between Rb concentration and G1 length and G1/S transition rate. We found that the Rb concentration at birth is positively correlated with G1 length (Figure 1E), and the Rb concentration is anti-correlated with the G1/S transition rate (Figure 1F). That these correlations are significant in Cdk-low cells but not in Cdk-high cells is consistent with Rb concentration regulating the G1/S transition only when Cdk activity is low. To further test this by exogenously controlling the concentration of Rb, we used HMEC cells containing a Dox-inducible allele of *RB1*. Increasing Rb concentration not only suppresses cell proliferation, but also further sensitizes cells to treatment by Cdk4/6 inhibitors (Figure 1G,H; Figure S2). Taken together, these experiments are consistent with our previous work and a recent study reporting that decreasing Rb concentration in G1 plays a crucial role in driving cells into the cell cycle in the absence of Cdk4/6 activity and facilitates the adaptation to chemical Cdk4/6 inhibitors [31].

Our findings demonstrate that Rb concentration more significantly impacts the cell cycle of cells with initially low Cdk activity. This makes sense because cells born with high Cdk activity likely quickly inactivate Rb via phosphorylation. This observation also explains why in many experiments overexpression of Rb does not have a big impact on cell proliferation [16,32]. This is likely because the majority of cells *in vitro* cultured cell lines, especially cancer cell lines, are in the Cdk-high category [25,32]. Even in the non-cancer cell lines, like the telomerase immortalized HMEC cells we used here, the majority of cells are born with high Cdk activity. However, this is not true in the cells growing *in vivo*. For example, the epidermal stem cells in mouse skin tissue have a much longer G1 duration than *in vitro* cultured cell lines and are not born with high Cdk activity[28,33]. Therefore, the Rb concentration is likely to have a bigger impact on cell cycle progression under *in vivo* settings.

Rb concentration dynamics are driven by cell cycle-dependent protein degradation

To identify the mechanism regulating Rb concentration dynamics through the cell cycle, we examined both the synthesis and degradation of Rb protein in different cell cycle phases. We measured the mRNA concentration of *RB1* in different cell cycle phases by using flow cytometry to sort HMEC cells expressing FUCCI [34] cell cycle reporters into G1 and S/G2 populations. We then performed qPCR and mRNA-Seq to measure *RB1* mRNA expression. The results showed that the *RB1* mRNA concentration did not significantly increase in S/G2 phase (Figure 2A, Figure S3A). We found a similar result when calculating *RB1* mRNA concentrations in different cell cycle phases using a published MERFISH dataset [35] (Figure S3B). This indicates that Rb concentration dynamics are controlled by post-transcriptional mechanisms. To further investigate the synthesis dynamics of Rb protein, we measured the translation efficiency of *RB1* mRNA by performing a RIP (RNA-binding protein immunoprecipitation) assay against the translation initiation factor eIF4E[77]. The relative translation efficiency is calculated by dividing the bound fraction of *RB1* with the bound fraction of housekeeping genes (*Actin* and *GAPDH*). Using this method, we found the relative translation efficiency of *RB1* was similar in sorted G1 and S/G2 cells as well as in asynchronously dividing and G1 arrested cells (Palbociclib treatment) (Figure 2B; Figure S3C). Taken together, our data indicate that Rb synthesis is not primarily responsible for its cell cycle dynamics.

Having found that Rb's cell cycle dynamics were not primarily due to transcription or translation mechanisms, we next sought to test if protein degradation was responsible. To do this, we utilized a doxycyclin (Dox)-inducible system in which cells conditionally express Clover-3xFlag-tagged Rb (*TRE-Clover-3xFlag-Rb*) or Clover-NLS (*TRE-Clover-NLS*) upon Dox treatment (1μg/mL). After 36h of Dox treatment, we withdrew Dox and monitored the decrease of the Clover fluorescence signal using live cell imaging (Figure S4A). Since the cells also express a FUCCI cell cycle marker, we can separately assess protein degradation taking place in G1 and S/G2 phases of the cell cycle (Figure S4A). By fitting the degradation traces using a simple exponential decay function, we obtained the half-life of Clover-3xFlag-Rb protein in different cell cycle phases for each cell. Rb half-life in early G1 (median 6.4h; 75% range 5.3h-9.4h) is significantly shorter than it is in S/G2 (median 37.3h, 75% range 29.2h-45.4h) (Figure 2C). The Rb tag location does not affect its half-life since a C-terminally tagged Rb protein (Rb-3xFlag-Clover) behaved similarly to the N-terminally tagged version (Figure 2D). The changing protein stability in G1 compared to S/G2 phases was specific to Rb as the short-lived Clover-NLS protein and stable Clover-NLS protein expressed with the same Dox-inducible system both had half-lives that did not change through the cell cycle (Figure 2D; Figure S4B, C). Thus, these results suggest a model where the Rb protein's cell cycle dynamics are due to its degradation in G1 and stabilization at the G1/S transition.

Having established that the regulation of Rb stability is most likely responsible for its cell cycle dynamics, we sought to test if this differential degradation of Rb is sufficient to give rise to the observed dynamics. To do this, we generated a mathematical model where only the half-life of the Rb protein changed through the cell cycle, while the synthesis rate remained constant (see methods). This simple model revealed that regulated degradation was sufficient to generate the cell-cycle dependent Rb concentration dynamics we observed, while the modest upregulation in the synthesis rate was insufficient (Figure 2E; Figure S4D). Note that the Rb protein 'dilution phenomenon' that we previously observed in [26], in which the total Rb protein amount is kept at a constant level during early G1 while the cell size is growing bigger, is a result of the changing balance between Rb synthesis and Rb being more actively degraded during early G1. From the model, we also examined the dynamics of total Rb protein amount, and we found that, with the experimental parameters for synthesis and degradation rates, the Rb protein amount is relatively constant in early G1 phase (Figure S4E). This shows that the observed dilution in G1 can be explained by Rb's degradation rate being similar to its synthesis rate in G1 while cell size increases. Taken together, our data and analysis indicate that the cell cycle-dependent regulation of Rb stability is primarily responsible for its cell cycle dynamics (Figure 2F).

Rb is stabilized via phosphorylation by Cdk

Having found that Rb is stabilized at the G1/S transition, we next sought to identify the molecular mechanism. One of the most prominent molecular changes occurring at the G1/S transition is the phosphorylation of Rb by Cyclin-Cdk complexes. We therefore sought to examine how Rb phosphorylation affected its half-life. To do this, we first stained asynchronous HMEC cells with phospho-Rb (S807/811) and total Rb antibodies. We then calculated the Rb concentration in the low phospho-Rb G1 population (low pRb G1), the high phospho-Rb G1 population (high pRb G1), and the S/G2 population. The Rb concentration is lower in early G1 when it is not hyper-phosphorylated and then begins to recover in late G1, when Rb is phosphorylated (Figure 3A). Similar results were obtained when G1 was partitioned into early and late phases using a recently published live-cell Cdk activity sensor (KTR sensor) based on the C-terminal part of Rb (886-928aa of Rb) [36] (Figure S5A). These immunofluorescence data support the model where the Rb concentration decrease in G1 phase is reversed upon its phosphorylation. Consistently, when cells are arrested in G1 by treating them with the Cdk4/6 inhibitor Palbociclib (1μM) for 24 hours, the Rb protein concentration drops by ~75% (Figure 3B) even though the mRNA concentration is only reduced by ~15% (Figure S5B). This is consistent with published results showing significant Rb protein drops when cells are exposed to Cdk4/6 inhibitors[37]. Furthermore, in cells expressing a Dox-inducible Clover-3xFlag-Rb protein, Palbociclib treatment led to a significant decrease in the concentration of this ectopically expressed protein but not the corresponding mRNA (Figure S5C). Taken together, these data suggest that the phosphorylation of Rb by Cdk mediates its stabilization. To test this model, we used the HDHB Cdk sensor to categorize cells into Cdk-low and Cdk-high populations before measuring the half-lives of Clover-Rb and Clover-NLS (Figure S5D, E). As anticipated, we found that Rb was degraded much more rapidly in the Cdk-low population.

To further investigate how Rb phosphorylation on different Cdk phosphorylation sites affects its half-life, we used the Dox-inducible system to express a series of Rb variants in which the Cdk phosphorylation sites were either substituted with non-phosphorylatable alanines or with phospho-mimetic double glutamic acid residues (EE) [38] (Figure S6A). For both mutant series, we extended the number of mutant sites from either the N- or C-terminus so that different mutants covered different parts of the protein (Figure S6A). If Cdk phosphorylation stabilizes Rb, then the phospho-mutants (S/T to A) should exhibit a reduced half-life in S/G2, and the phospho-mimetic mutants (S/TP to EE) should exhibit an increased half-life in early G1. Our

results are consistent with this hypothesis (Figure 3C, D; Figure S6B, C). It is worth noting that the C-terminal alanine-mutants also had a more severe cell cycle arrest phenotype (Figure S7A). This is likely because the alanine mutants do not allow the phosphorylation of C-terminal residues to disrupt Rb's interaction with E2F-DP [11,12,29,39]. On the other hand, the phospho-mimetic mutants did not demonstrate significant cell cycle defects (Figure S7B), likely because these Rb mutants are partially or entirely unable to bind and inhibit E2F. In addition, the introduction of phospho-mimetic mutations resulted in a smaller Rb concentration decrease in cells arrested in G1 using Palbociclib (Figure S7C, D).

Interestingly, our mutational analysis did not reveal any particular phosphorylation sites that predominantly regulated Rb's half-life (Figure 3E, F; Figure S6C; Figure S7C, D). Instead, the degree of Rb stabilization, the ratio between early G1 and S/G2 half-lives, correlated with the total number of phospho-mimetic sites. This shows that many different phosphorylation sites contribute to Rb stability. We note that Rb14EE exhibited reduced half-lives for both early G1 and S/G2 phases, which is likely due to the additional SP230EE mutation destabilizing the protein via another mechanism (Figure 3E; Figure S7D). However, the difference between early G1 and S/G2 half-lives in Rb14EE is the smallest (Figure S6C). Collectively, these results support the hypothesis that Rb is stabilized by its hyper-phosphorylation in late G1 by Cdk (Figure 3G).

The degradation of un- or hypo-phosphorylated Rb is mediated by the E3 ubiquitin ligase UBR5

After establishing that Rb is stabilized by phosphorylation at the G1/S transition, we next sought to identify the underlying molecular mechanism. To do this, we first tested whether Rb is degraded through the ubiquitin-proteasome system by treating cells with three commonly used inhibitors of different components of this degradation system: Bortezomib inhibits the proteasome; TAK243 inhibits the ubiquitin activating enzyme (E1); and MLN4924 inhibits the NEDD8-activating enzyme that activates the Cullin (CUL)-RING E3 ubiquitin ligases [40,41]. We treated asynchronously growing HMEC cells with these inhibitors for 5 hours, and then immunostained the cells using antibodies for pRb (S807/811) and total Rb. TAK243 and Bortezomib treatments increased the Rb concentration in the low pRb G1 populations to a level similar to that in the high pRb G1 population, but MLN4924 did not (Figure S8A, B). RPE-1 cells (telomerase immortalized retinal pigment epithelium cells) behaved similarly to HMEC cells in that only TAK243 and Bortezomib treatments increased the Rb concentration in the low pRb G1 population (Figure S8C). To further confirm that the phosphorylation status determines Rb degradation through the ubiquitin-proteasome system, we treated cells that were induced to express un-phosphorylated Rb that lacks all the Cdk phosphorylation sites (Clover-3xFlag-RbΔCDK) or phospho-mimetic Rb (Clover-3xFlag-Rb14EE) with the three degradation inhibitors discussed above. The concentration of RbΔCDK is elevated by TAK243 and Bortezomib, but not MLN4924, and the concentration of Rb14EE does not increase following treatment by any of the three inhibitors (Figure 4A). We also confirmed the enhanced ubiquitination of RbΔCDK by pulling down Clover-3xFlag-RbΔCDK and blotting for ubiquitin. RbΔCDK was more ubiquitinated than WT Rb, which is mostly in the hyper-phosphorylated form (Figure 4B). Altogether, these data suggest that un-phosphorylated Rb is degraded in G1 through the ubiquitin-proteasome system, but not by the Cullin (CUL)-RING E3 ligases.

There have been several previous studies of Rb degradation mechanisms that identified some E3 ligases [37,42–49]. For example, MDM2 may mediate Rb degradation via its central acidic domain [42,43,47]. The human papilloma virus (HPV) E7 protein can bind Rb and induce its degradation [46], which is mediated by protease cleavage at Lys810 [44]. More recently, Cdk4/6

282 inhibition was found to promote Rb degradation through βTrCP1-mediated ubiquitination [37]. To
283 test if these E3 ligases were responsible for the observed cell cycle dynamics of Rb, we
284 examined the effect of knocking them down on the concentration of un-phosphorylated Rb
285 (Clover-3xFlag-RbΔCDK) and phospho-mimetic Rb (Clover-3xFlag-Rb14EE). If an E3 were
286 responsible for Rb's cell cycle dynamics, we would expect to see an increase in the
287 concentration of Clover-3xFlag-RbΔCDK but not of Clover-3xFlag-Rb14EE. None of the
288 knockdowns exhibited this predicted phenotype (Figure S9A). Even through some of the
289 knockdowns affected the overall Rb concentration, this effect was not specific for un-
290 phosphorylated Rb and therefore could not explain Rb's cell cycle dynamics. Similarly, we
291 performed the same set of knockdowns in cells arrested in G1 using Palbociclib and did not find
292 any specific increase in the concentrations of un- or hypo-phosphorylated Rb (Figure S9B-G).
293 This implies that there must be some additional E3 ligase responsible for the phosphorylation-
294 dependent degradation of Rb.
295
296 To identify the E3 ligases mediating the degradation of un-phosphorylated Rb, we set up an
297 siRNA screen. We used a customized siRNA library that included the previously published E3
298 ligases for Rb, some nuclear localized E3s (according to UniProt), and some additional genes
299 predicted to be E3 ligases for Rb (http://ubibrowser.bio-it.cn/ubibrowser_v3/) (Figure 4C). HMEC
300 cells inducibly expressing Clover-3xFlag-RbΔCDK or Clover-3xFlag-Rb14EE were transfected
301 with the siRNA library. 48 hours later, cells were fixed and imaged. The concentration of Clover-
302 3xFlag-Rb variants was measured in each treatment and its fold change over non-transfected
303 cells was calculated. As positive controls, we included the ubiquitin-proteasome system
304 inhibitors TAK243 and Bortezomib. As expected, TAK243 and Bortezomib only increased the
305 concentration of RbΔCDK but not Rb14EE (Figure 4D; Figure S10A, B). From this screen, we
306 only identified UBR5 as specifically targeting un-phosphorylated Rb for degradation (Figure 4D;
307 Figure S10A, B). UBR5 is a verified E3 ubiquitin ligase belonging to the HECT family known to
308 play roles in transcription and the DNA damage response [50–53]. However, Rb has never been
309 reported to be a substrate of UBR5. To confirm that UBR5 is the main E3 ligase targeting un-
310 phosphorylated Rb, we first performed another siRNA screen with a different siRNA library
311 containing UBR5 and 17 other E3 genes from the first library as well as the rest of the nuclear
312 localized E3 genes not included in the first screen. We also included several E1 and E2 genes
313 (Figure 4C). This second siRNA screen also only identified UBR5 (Figure 4E; Figure S10B-D).
314
315 We then validated UBR5 as a hit using another two independent siRNAs against UBR5.
316 Knockdown of UBR5 in HMEC cells led to the accumulation of un/hypo-phosphorylated Rb after
317 Palbociclib treatment, as measured by both immunoblot and immunostaining (Figure 5A, Figure
318 S11A). We also measured the half-life of Rb following UBR5 knockdown using live-cell imaging
319 and found that Rb was degraded about twice as slowly in early G1, but there was no change in
320 its stability in S/G2, as compared to the control siRNA (Figure 5B). Moreover, we examined the
321 effect of knocking down UBR5 on HMEC cells expressing endogenously tagged Rb (*RB1-*
322 *3xFLAG-Clover-sfGFP*)[26]. Following *UBR5* knockdown, the concentration of Rb does not
323 decrease in early G1, but is instead kept relatively constant (Figure S11B). To further confirm
324 that the degradation of un-phosphorylated Rb by UBR5 is not cell line or cell type specific, we
325 also examined epithelial RPE-1 cells as well as HLF (primary human lung fibroblast) and T98G
326 (glioblastoma-derived fibroblast-like) cells. All of them showed that UBR5 knockdown increased
327 concentrations of un- and hypo-phosphorylated Rb in Palbociclib-treated cells (Figure S11C-E).
328
329 After establishing that Rb degradation depends on UBR5, we sought to test for a direct
330 interaction between these two proteins. To do this, we performed immunoprecipitation assays
331 with UBR5 and un-phosphorylated Rb, wild-type Rb, and phospho-mimetic Rb. We found that
332 the un-phosphorylated Rb, which lacks all Cdk sites, can pull down significantly more UBR5

333 than wild-type Rb. Moreover, the phospho-mimetic Rb pulled down the smallest amount of
334 UBR5 (Figure 5C). This result showing a direct phosphorylation-dependent interaction, is
335 consistent with our hypothesis that UBR5 targets un-phosphorylated Rb for degradation, and Rb
336 phosphorylation protects Rb from UBR5-dependent degradation.
337
338 To test if UBR5 mediated Rb degradation *in vivo*, we examined its effect in the mouse liver
339 using the *Fah-/-* system[54,55]. In the *Fah-/-* system, deletion of the *Fah* gene causes toxin
340 accumulation in hepatocytes that will lead to hepatocyte death. Toxin accumulation can be
341 prevented by treating mice with NTBC (2-(2-nitro-4-trifluoromethylbenzoyl)-1,3-
342 cyclohexanedione)[55]. When NTBC is withdrawn, cells expressing exogenous *Fah*, introduced by
343 injecting *Fah*+ transposons, will clonally expand to repopulate the injured liver [55] (Figure 5D).
344 Importantly, other genetic elements, such as Cas9 and gRNA, can be added to the *Fah*
345 transposon so that they are co-integrated into some hepatocyte genomes. To knock out *Ubr5* in
346 some hepatocytes, we modified an *Fah* transposon plasmid [56] and delivered *Fah-P2A-Cas9-*
347 *sgUbr5* or *Fah-P2A-Cas9-sgNT* (non-targeting) transposons and the SB100 transposase into
348 *Fah-/-* mice via hydrodynamic transfection. 8 weeks after injection, when the liver was almost
349 fully repopulated with *Fah*+ cells, we isolated the hepatocytes, plated them, and performed
350 immunostaining or immunoblots (Figure S11F). Consistent with the results from human cell
351 lines, knocking out *Ubr5* increased Rb concentrations in mouse hepatocytes where Rb was not
352 hyper-phosphorylated (low pRb) (Figure 5D, Figure S11G, H). The results from this *Fah-/- in*
353 *vivo* model further support our conclusion that the E3 ligase UBR5 targets un-phosphorylated
354 Rb for degradation in G1 (Figure 5E).
355
356 Our results here give insight into why previous studies reported other E3s targeting Rb. First,
357 any E3 whose knockdown results in a cell cycle phenotype would be predicted to have an effect
358 on Rb concentration. Second, after finding Rb dynamics were driven by the degradation of un-
359 or hypo-phosphorylated Rb in G1, we sought to find E3s that specifically targeted the un-
360 phosphorylated RbΔCDK protein, but not the phospho-mimetic Rb14EE protein. We did find a
361 significant increase in both RbΔCDK and Rb14EE when the E3 MDM2 was knocked down, and
362 possibly very modest effects when other reported E3s were knocked down (Figure S9A; Figure
363 S10A). This suggests that these other E3s might operate in different cell types or contexts, but
364 are not generally responsible for Rb's cell cycle dynamics.
365
366 **UBR5 and Cdk4/6 drive parallel pathways promoting the G1/S transition**
367
368 It is becoming increasingly clear that there are two distinct pathways driving the G1/S transition
369 that both operate through Rb. First, the canonical Cdk-phosphorylation pathway through which
370 Cyclin D-Cdk4/6 complexes phosphorylate and inhibit Rb, and second, the Rb-degradation
371 pathway that drives down the concentration of Rb in G1 phase. One prediction from this parallel
372 pathway model is that cells lacking the Rb-degradation pathway should be more sensitive to
373 inhibition of the remaining Rb-phosphorylation pathway. We can now test this prediction
374 because we identified UBR5 as the E3 ligase targeting un-phosphorylated Rb in G1. To do this,
375 we first generated clonal cell lines lacking *UBR5* from HMEC cells using CRISPR/Cas9. We
376 randomly picked three *UBR5 WT* clones and three *UBR5 KO* clones for analysis (Figure 6A).
377 *UBR5 KO* cells exhibited higher Rb concentrations in low pRb G1 cells (Figure 6B; Figure
378 S12A). Moreover, *UBR5 KO* cells also exhibited both higher endogenous Rb concentrations and
379 higher exogenous Clover-3xFlag-Rb concentrations following Palbociclib treatment to arrest
380 cells in G1 (Figure S12B, C; Figure S14A, B). *UBR5 KO* cells also exhibited increases in Rb
381 half-life in early G1 (Figure 6C; Figure S13A, B), and exhibited increases in the half-life of un-
382 phosphorylated RbΔCDK, but not phospho-mimetic Rb14EE, as measured by our live-cell

383 imaging assay (Figure 6D; Figure S13C, D). These knockout lines therefore exhibited all the
384 same effects we observed in our earlier knockdown experiments shown in Figure 5.
385
386 Having generated *UBR5 KO* cells, we are can now test the parallel pathway model prediction
387 that cells lacking the Rb-degradation pathway are more sensitive to inhibition of the Rb-
388 phosphorylation pathway. To do this, we treated *UBR5 WT* and *UBR5 KO* cells with the Cdk4/6
389 inhibitor Palbociclib for 72 hours and then measured cell proliferation by counting cell numbers.
390 Since different clonal cell lines had different proliferation rates to begin with (Figure S15A), we
391 normalized the cell numbers of Palbociclib treated cells to the cell numbers in the DMSO control
392 treatment for each clonal cell line. Moreover, this normalization also accounts for the slower
393 growth rates of *UBR5 KO* cells (Figure S15A) that are likely due to the dysregulation of other
394 UBR5 substrates. As predicted by the parallel pathway model, *UBR5 KO* cells are more
395 sensitive to Palbociclib treatment than *UBR5 WT* cells (Figure 6E, Figure S15A). To further
396 determine the proliferation status of *UBR5 WT* and *KO* cells, we also stained the cells with
397 phospho-Rb antibodies following prolonged DMSO or Palbociclib treatments up to 6 days. As
398 expected, a significantly higher proportion of *UBR5 WT* cells were progressing through the cell
399 cycle (as indicated by cells having hyper-phosphorylated Rb) compared to *UBR5 KO* cells,
400 again supporting the parallel pathway model (Figure S15B-E).
401
402 Since UBR5 has other substrates that may also affect cell cycle progression, we wanted to
403 examine if UBR5 KO cells' increased sensitivity to Palbociclib treatment was due to the
404 stabilization of Rb. To test this, we knocked out *RB1* in *UBR5 KO* cells using CRISPR/Cas9
405 (Figure S16A) and tested their sensitivity to Palbociclib treatment. Knocking out *RB1* in *UBR5*
406 *KO* cells completely rescued the increased Palbociclib sensitivity exhibited by *UBR5 KO* cells
407 (Figure 6F; Figure S16B), suggesting that the effect of UBR5 on the G1/S transition is primarily
408 through the stabilization of Rb. Lastly, to make sure that the effect of UBR5 on cell cycle
409 progression was due to its E3 ligase activity, we added back either wild-type UBR5 or an
410 inactive mutant UBR5 to the *UBR5 KO* cells using the Dox-inducible system (Figure S17A). The
411 mutant UBR5 has a C2768A mutation in the HECT domain (abbreviated as UBR5ΔHECT),
412 which kills its catalytic activity [51]. Consistent with the role of UBR5 degrading un-phosphorylated
413 Rb, the expression of UBR5 WT was able to reduce Rb concentration in the low pRb G1
414 population in *UBR5 KO* cells, but expressing UBR5ΔHECT did not (Figure 6G; Figure S17B, C).
415 We treated cells expressing UBR5 WT or UBR5ΔHECT (induced by Dox) with DMSO or
416 Palbociclib for 72 hours, and found that adding back UBR5 WT decreased the cells' Palbociclib
417 sensitivity compared to the no Dox control, whereas adding back the UBR5ΔHECT did not
418 (Figure 6H; Figure S18A, B). This indicates that the E3 ligase activity of UBR5 is essential for its
419 function as a key component of the Rb-degradation pathway.
420
421 Since deleting UBR5 sensitizes cells to treatment by Cdk4/6 inhibitors that are currently used to
422 target breast cancers, we next explored if UBR5 itself could be a potential therapeutics target. To
423 do this, we examined the *UBR5* copy number level in breast cancer patients and how it relates to
424 the patient's survival. Since there is a lot of variability between patients depending on the
425 molecular basis of their disease, we categorized patients for analysis using the Integrative Cluster
426 subtype (IC) framework that partitions groups of patients based on multiple types of genomic data
427 [57,58]. IC subtypes predict patient outcomes beyond the historical clinical stratification based on
428 hormone receptors status: ER+, HER2+, and triple-negative subgroups [57,58]. IC classification
429 stratifies ER+ tumors into ER+ Typical-risk (IC3,4ER+,7,8) and ER+ High-risk of relapse
430 (IC1,2,6,9) categories, and stratifies triple-negative tumors (TNBC) into the genomically stable
431 and unstable subtypes IC4ER- and IC10, respectively [57,57]. Among the 1894 patient samples from
432 the Molecular Taxonomy of Breast Cancer International Consortium (METABRIC), the *UBR5*
433 gene was amplified in the majority of the patients. When stratified by the prognostic subtypes,

UBR5 gene copy amplification was observed in all subgroups but to various degrees (Figure 6I; Figure S18C). Importantly, *UBR5* amplification was particularly dominant in subgroups associated with a worse prognosis (ER+ High-risk, HER2+, and TNBC tumors). We then assessed how *UBR5* gene copy alteration affected patient survival. By analyzing the distant relapse-free (DRF) survival of these patients, we found that *UBR5* amplification is associated with worse DRF survival (Figure 6J), especially in IC1 (ER+ High-risk) and IC10 (TNBC, basal-like tumors) subtypes (Figure 6J). These results suggest that breast cancer cells might increase *UBR5* expression through copy number amplification to facilitate cell cycle progression.

Discussion

Two distinct pathways drive the G1/S transition by reducing the activity and amount of the key cell cycle inhibitor Rb: the canonical Cdk-phosphorylation pathway and the Rb-degradation pathway (Figure 7). Here, we report that the Rb-degradation pathway is driven by the E3 ubiquitin ligase UBR5 and is shut off by Rb hyper-phosphorylation in late G1. This mechanism could explain why some cells can still progress into S phase and activate Cdk2 even when Cdk4/6 is being inhibited [7]. Namely, when Cdk4/6 activity is inhibited in cells, protein degradation continuously decreases the Rb concentration. This eventually leads to partial activation of E2F-dependent transcription, which activates Cyclin E/A-Cdk2 to hyper-phosphorylate Rb and drive S phase entry. Therefore, the Rb degradation pathway provides cells with an alternative path to enter the division cycle, emphasizing the plasticity of the cell cycle program that is likely important in different cell types and contexts.

While the two pathways impinging on Rb activity employ distinct mechanisms, degradation and phosphorylation, their activities become interconnected once cells begin the G1/S transition. Namely, the degradation of Rb eventually drives an increase in E2F activity and thereby transcription of Cyclin A and Cyclin E. These downstream cyclins can then form a complex with Cdk2 to drive Rb hyper-phosphorylation and stabilization. Consequently, Rb degradation drives Cdk activity, which in turn inhibits Rb degradation as cells progress into S phase. Nevertheless, while these activities become interconnected at the restriction point and the G1/S transition, prior to this point it is likely that they operate independently so that UBR5 and Cyclin D-Cdk4/6 activities can be separately modulated to control the timing of the G1/S transition in a variety of cellular contexts.

The parallel pathway model predicts that cells with low Cdk activity will more heavily rely on the Rb-degradation pathway to facilitate their G1/S transition. This prediction is supported by our live-cell imaging results (Figure 1). As reported previously, we see many cultured cells immediately activating Cdk activity (Cdk-high), while some other cells have a longer G1 period with lower Cdk activity (Cdk-low) [1,25]. In Cdk-low cells, the Rb concentration continually decreases in G1 until a couple of hours before S phase. Moreover, the Rb concentration in G1 negatively correlates with the G1/S transition rate. While manipulating Rb concentration has minor effects on cell proliferation in many cancer cell lines and immortalized cell lines [16,32], this is likely due to the high Cdk activity in these cells and the rich *in vitro* culture environment. Consistent with this view, Rb concentration is not important in Cdk-high activity cells, which are the majority in most *in vitro* cultured cell lines. The cell cycle dynamics of cultured cells stands in sharp contrast to the dynamics of cells proliferating *in vivo*. For example, the epidermal stem cells in mouse skin have a G1 length around 48-72 hours[28,33], far exceeding the G1 length in *in vitro* cultured cell lines [1,2,25]. Thus, cells proliferating *in vivo* are likely more similar to the Cdk-low cells and therefore are expected to rely on the Rb degradation pathway. Indeed, manipulation of the Rb-pathway in mouse epidermal stem cells regulates their G1 dynamics[28].

While we identified UBR5 as the E3 ligase that targets Rb for degradation, we want to emphasize that Rb is not the sole target of UBR5. Multiple papers have shown that UBR5 has other targets including MYC, Nuclear hormone receptors, and SPT4/5 [51–53]. Here, we identify Rb as an additional target of UBR5. Yet, the mechanism through which UBR5 recognizes Rb is still unclear. UBR5 likely engages its substrates as a dimer or tetramer, which can target distinct degron linear motifs as indicated by recent cryo-EM structures [52,53,59–61]. Since UBR5 is a large multi-domain protein, it is possible that different docking mechanisms can be utilized for engaging different groups of substrates [51,53,60–62]. Interestingly, two recent studies proposed that UBR5 targets its substrates on chromatin [52,53]. This possible preference of UBR5 for chromatin-bound targets might explain the results of our mutational analysis of Rb. Namely, the more tightly an Rb variant is predicted to bind the E2F transcription factor, the more rapidly it is degraded. The Rb variants with increasing numbers of phospho-mimetic sites (Figure 3E; Figure S6A, C) have decreasing binding affinity to E2F (and chromatin), and exhibited increasing stability in G1. In support of such a model, the stabilization of Rb at the G1/S transition is coincident with its hyper-phosphorylation and dissociation from the chromatin-bound E2F transcription factors [63].

UBR5, like other components of the canonical Rb-phosphorylation pathway, appears frequently mutated in cancer and may become a target for therapies [64]. For example, Cdk4/6 inhibitors in combination with endocrine therapy are used to treat advanced estrogen receptor positive (ER+)/human epidermal growth factor receptor-2 negative (HER2-) breast cancers [65–67]. However, this application is frequently limited by the intrinsic and acquired therapeutic resistance observed in patients [68,69]. One possible way to improve upon current therapies targeting the Rb-phosphorylation pathway is to also target the Rb-degradation pathway through UBR5. Since deleting UBR5 sensitizes cells to treatment by Cdk4/6 inhibitors, it is possible that current Cdk4/6 inhibitor-based treatments for breast cancer can be improved by developing novel therapeutics targeting the Rb-degradation pathway through UBR5, which, intriguingly, is frequently amplified in such cancers (Figure 6I).

The inability of current therapies to inhibit cell division reflects our incomplete knowledge of the signaling pathways involved. During G1 phase, the cell integrates many signals to make the decision to commit to cell division including two separate signaling pathways targeting Rb. The existence of these two parallel pathways explains the ability of some cells to proliferate in the absence of Cyclin D-dependent kinase activity [7,70,71]. Namely, these cells rely more heavily on the UBR5-Rb degradation pathway than the canonical Cdk4/6 Rb-phosphorylation pathway. In addition to providing such a robust entry to the cell division cycle in a particular cellular context, the existence of parallel pathways regulating the G1/S transition might be due to the different proliferative requirements of diverse cell types [72]. Different pathways can be independently tuned to precisely calibrate the rate of proliferation required by the myriad cell types and niches of a multicellular organism. Discovering the mechanisms underlying these G1/S regulatory pathways, such as we have here for Rb-degradation, will therefore give insight into both development and disease.

527 **References**
528

529 1. Schwarz, C., Johnson, A., Kõivomägi, M., Zatulovskiy, E., Kravitz, C.J., Doncic, A., and
530 Skotheim, J.M. (2018). A Precise Cdk Activity Threshold Determines Passage through the
531 Restriction Point. Mol Cell *69*, 253-264.e5. 10.1016/j.molcel.2017.12.017.

532 2. Cappell, S.D., Chung, M., Jaimovich, A., Spencer, S.L., and Meyer, T. (2016). Irreversible
533 APCCdh1 Inactivation Underlies the Point of No Return for Cell-Cycle Entry. Cell *166*, 167–
534 180. 10.1016/j.cell.2016.05.077.

535 3. Moser, J., Miller, I., Carter, D., and Spencer, S.L. (2018). Control of the Restriction Point by
536 Rb and p21. Proceedings of the National Academy of Sciences *115*, E8219–E8227.
537 10.1073/pnas.1722446115.

538 4. Zetterberg, A., Larsson, O., and Wiman, K.G. (1995). What is the restriction point? Curr
539 Opin Cell Biol *7*, 835–842. 10.1016/0955-0674(95)80067-0.

540 5. Rubin, S.M., Sage, J., and Skotheim, J.M. (2020). Integrating Old and New Paradigms of
541 G1/S Control. Mol Cell *80*, 183–192. 10.1016/j.molcel.2020.08.020.

542 6. Chung, M., Liu, C., Yang, H.W., Köberlin, M.S., Cappell, S.D., and Meyer, T. (2019).
543 Transient Hysteresis in CDK4/6 Activity Underlies Passage of the Restriction Point in G1.
544 Molecular Cell *76*, 562-573.e4. 10.1016/j.molcel.2019.08.020.

545 7. Liu, C., Konagaya, Y., Chung, M., Daigh, L.H., Fan, Y., Yang, H.W., Terai, K., Matsuda, M.,
546 and Meyer, T. (2020). Altered G1 signaling order and commitment point in cells proliferating
547 without CDK4/6 activity. Nat Commun *11*, 5305. 10.1038/s41467-020-18966-9.

548 8. Cappell, S.D., Mark, K.G., Garbett, D., Pack, L.R., Rape, M., and Meyer, T. (2018). EMI1
549 switches from being a substrate to an inhibitor of APC/CCDH1 to start the cell cycle. Nature
550 *558*, 313–317. 10.1038/s41586-018-0199-7.

551 9. Rubin, S.M. (2013). Deciphering the Rb phosphorylation code. Trends Biochem Sci *38*, 12–
552 19. 10.1016/j.tibs.2012.10.007.

553 10. Mittnacht, S. (1998). Control of pRB phosphorylation. Current Opinion in Genetics &
554 Development *8*, 21–27. 10.1016/S0959-437X(98)80057-9.

555 11. Knudsen, E.S., and Wang, J.Y. (1997). Dual mechanisms for the inhibition of E2F binding to
556 RB by cyclin-dependent kinase-mediated RB phosphorylation. Mol Cell Biol *17*, 5771–5783.
557 10.1128/MCB.17.10.5771.

558 12. Brown, V.D., Phillips, R.A., and Gallie, B.L. (1999). Cumulative Effect of Phosphorylation of
559 pRB on Regulation of E2F Activity. Mol Cell Biol *19*, 3246–3256.

560 13. Winston, J.T., and Pledger, W.J. (1993). Growth factor regulation of cyclin D1 mRNA
561 expression through protein synthesis-dependent and -independent mechanisms. Mol Biol
562 Cell *4*, 1133–1144.

563 14. Fassl, A., Geng, Y., and Sicinski, P. (2022). CDK4 and CDK6 kinases: From basic science
564 to cancer therapy. Science *375*, eabc1495. 10.1126/science.abc1495.

565 15. Narasimha, A.M., Kaulich, M., Shapiro, G.S., Choi, Y.J., Sicinski, P., and Dowdy, S.F.
566 (2014). Cyclin D activates the Rb tumor suppressor by mono-phosphorylation. eLife *3*,
567 e02872. 10.7554/eLife.02872.

568 16. Sanidas, I., Morris, R., Fella, K.A., Rumde, P.H., Boukhali, M., Tai, E.C., Ting, D.T.,
569 Lawrence, M.S., Haas, W., and Dyson, N.J. (2019). A Code of Mono-phosphorylation
570 Modulates the Function of RB. Mol Cell *73*, 985-1000.e6. 10.1016/j.molcel.2019.01.004.

571 17. Barnes, D.M., and Gillett, C.E. (1998). Cyclin D1 in Breast Cancer. Breast Cancer Res Treat
572 *52*, 1–15. 10.1023/A:1006103831990.

573 18. Musgrove, E.A., Caldon, C.E., Barraclough, J., Stone, A., and Sutherland, R.L. (2011).
574 Cyclin D as a therapeutic target in cancer. Nat Rev Cancer *11*, 558–572. 10.1038/nrc3090.

575 19. Ewen, M.E., and Lamb, J. (2004). The activities of cyclin D1 that drive tumorigenesis.
576 Trends in Molecular Medicine *10*, 158–162. 10.1016/j.molmed.2004.02.005.

577 20. Reissmann, P.T., Koga, H., Figlin, R.A., Holmes, E.C., Slamon, D.J., and The Lung Cancer
578 Study Group (1999). Amplification and overexpression of the cyclin D1 and epidermal
579 growth factor receptor genes in non-small-cell lung cancer. J Cancer Res Clin Oncol *125*,
580 61–70. 10.1007/s004320050243.

581 21. Jiang, W., Kahn, S.M., Tomita, N., Zhang, Y.-J., Lu, S.-H., and Weinstein, I.B. (1992).
582 Amplification and Expression of the Human Cyclin D Gene in Esophageal Cancer1. Cancer
583 Research *52*, 2980–2983.

584 22. Jeffreys, S.A., Becker, T.M., Khan, S., Soon, P., Neubauer, H., de Souza, P., and Powter,
585 B. (2022). Prognostic and Predictive Value of CCND1/Cyclin D1 Amplification in Breast
586 Cancer With a Focus on Postmenopausal Patients: A Systematic Review and Meta-
587 Analysis. Front Endocrinol (Lausanne) *13*, 895729. 10.3389/fendo.2022.895729.

588 23. Fukuda, T., Furuya, K., Takahashi, K., Orimoto, A., Sugano, E., Tomita, H., Kashiwagi, S.,
589 Kiyono, T., and Ishii, T. (2021). Combinatorial expression of cell cycle regulators is more
590 suitable for immortalization than oncogenic methods in dermal papilla cells. iScience *24*,
591 101929. 10.1016/j.isci.2020.101929.

592 24. Ramirez, R.D., Herbert, B.-S., Vaughan, M.B., Zou, Y., Gandia, K., Morales, C.P., Wright,
593 W.E., and Shay, J.W. (2003). Bypass of telomere-dependent replicative senescence (M1)
594 upon overexpression of Cdk4 in normal human epithelial cells. Oncogene *22*, 433–444.
595 10.1038/sj.onc.1206046.

596 25. Spencer, S.L., Cappell, S.D., Tsai, F.-C., Overton, K.W., Wang, C.L., and Meyer, T. (2013).
597 The proliferation-quiescence decision is controlled by a bifurcation in CDK2 activity at
598 mitotic exit. Cell *155*, 369–383. 10.1016/j.cell.2013.08.062.

599 26. Zatulovskiy, E., Zhang, S., Berenson, D.F., Topacio, B.R., and Skotheim, J.M. (2020). Cell
600 growth dilutes the cell cycle inhibitor Rb to trigger cell division. Science *369*, 466–471.

601 27. Zhang, S., Zatulovskiy, E., Arand, J., Sage, J., and Skotheim, J.M. (2022). The cell cycle
602 inhibitor RB is diluted in G1 and contributes to controlling cell size in the mouse liver.
603 Preprint at bioRxiv, 10.1101/2022.06.08.495371 10.1101/2022.06.08.495371.

604 28. Xie, S., Zhang, S., Medeiros, G.Q.G. de, Liberali, P., and Skotheim, J. (2024). The G1/S
605 transition in mammalian stem cells in vivo is autonomously regulated by cell size. Preprint at
606 bioRxiv, 10.1101/2024.04.09.588781 10.1101/2024.04.09.588781.

607 29. Topacio, B.R., Zatulovskiy, E., Cristea, S., Xie, S., Tambo, C.S., Rubin, S.M., Sage, J.,
608 Kõivomägi, M., and Skotheim, J.M. (2019). Cyclin D-Cdk4,6 Drives Cell-Cycle Progression
609 via the Retinoblastoma Protein's C-Terminal Helix. Mol Cell *74*, 758-770.e4.
610 10.1016/j.molcel.2019.03.020.

611 30. Sun, X., Bizhanova, A., Matheson, T.D., Yu, J., Zhu, L.J., and Kaufman, P.D. (2017). Ki-67
612 Contributes to Normal Cell Cycle Progression and Inactive X Heterochromatin in p21
613 Checkpoint-Proficient Human Cells. Molecular and Cellular Biology *37*, e00569-16.
614 10.1128/MCB.00569-16.

615 31. Zhang, M., Kim, S., and Yang, H.W. (2023). Non-canonical pathway for Rb inactivation and
616 external signaling coordinate cell-cycle entry without CDK4/6 activity. Nat Commun *14*,
617 7847. 10.1038/s41467-023-43716-y.

618 32. Broceño, C., Wilkie, S., and Mittnacht, S. (2002). RB activation defect in tumor cell lines.
619 Proceedings of the National Academy of Sciences *99*, 14200–14205.
620 10.1073/pnas.212519499.

621 33. Xie, S., and Skotheim, J.M. (2020). A G1 Sizer Coordinates Growth and Division in the
622 Mouse Epidermis. Current Biology *30*, 916-924.e2. 10.1016/j.cub.2019.12.062.

623 34. Sakaue-Sawano, A., Kurokawa, H., Morimura, T., Hanyu, A., Hama, H., Osawa, H.,
624 Kashiwagi, S., Fukami, K., Miyata, T., Miyoshi, H., et al. (2008). Visualizing Spatiotemporal
625 Dynamics of Multicellular Cell-Cycle Progression. Cell *132*, 487–498.
626 10.1016/j.cell.2007.12.033.

627 35. Xia, C., Fan, J., Emanuel, G., Hao, J., and Zhuang, X. (2019). Spatial transcriptome profiling
628 by MERFISH reveals subcellular RNA compartmentalization and cell cycle-dependent gene
629 expression. Proceedings of the National Academy of Sciences *116*, 19490–19499.
630 10.1073/pnas.1912459116.

631 36. Yang, H.W., Cappell, S.D., Jaimovich, A., Liu, C., Chung, M., Daigh, L.H., Pack, L.R., Fan,
632 Y., Regot, S., Covert, M., et al. (2020). Stress-mediated exit to quiescence restricted by
633 increasing persistence in CDK4/6 activation. eLife *9*, e44571. 10.7554/eLife.44571.

634 37. Dang, F., Nie, L., Zhou, J., Shimizu, K., Chu, C., Wu, Z., Fassl, A., Ke, S., Wang, Y., Zhang,
635 J., et al. (2021). Inhibition of CK1ε potentiates the therapeutic efficacy of CDK4/6 inhibitor in
636 breast cancer. Nat Commun *12*, 5386. 10.1038/s41467-021-25700-6.

637 38. Repetto, M.V., Winters, M.J., Bush, A., Reiter, W., Hollenstein, D.M., Ammerer, G., Pryciak,
638 P.M., and Colman-Lerner, A. (2018). CDK and MAPK Synergistically Regulate Signaling
639 Dynamics via a Shared Multi-site Phosphorylation Region on the Scaffold Protein Ste5.
640 Molecular Cell *69*, 938-952.e6. 10.1016/j.molcel.2018.02.018.

641 39. Burke, J.R., Liban, T.J., Restrepo, T., Lee, H.-W., and Rubin, S.M. (2014). Multiple
642 Mechanisms for E2F Binding Inhibition by Phosphorylation of the Retinoblastoma Protein C-
643 Terminal Domain. Journal of Molecular Biology *426*, 245–255. 10.1016/j.jmb.2013.09.031.

644 40. Deshaies, R.J., Emberley, E.D., and Saha, A. (2010). Control of cullin-ring ubiquitin ligase
645 activity by nedd8. Subcell Biochem *54*, 41–56. 10.1007/978-1-4419-6676-6_4.

646 41. Luo, Z., Pan, Y., Jeong, L.S., Liu, J., and Jia, L. (2012). Inactivation of the Cullin (CUL)-
647 RING E3 ligase by the NEDD8-activating enzyme inhibitor MLN4924 triggers protective
648 autophagy in cancer cells. Autophagy *8*, 1677–1679. 10.4161/auto.21484.

649 42. Sdek, P., Ying, H., Zheng, H., Margulis, A., Tang, X., Tian, K., and Xiao, Z.-X.J. (2004). The
650 central acidic domain of MDM2 is critical in inhibition of retinoblastoma-mediated
651 suppression of E2F and cell growth. J Biol Chem *279*, 53317–53322.
652 10.1074/jbc.M406062200.

653 43. Sdek, P., Ying, H., Chang, D.L.F., Qiu, W., Zheng, H., Touitou, R., Allday, M.J., and Xiao,
654 Z.-X.J. (2005). MDM2 Promotes Proteasome-Dependent Ubiquitin-Independent
655 Degradation of Retinoblastoma Protein. Molecular Cell *20*, 699–708.
656 10.1016/j.molcel.2005.10.017.

657 44. Tomita, T., Huibregtse, J.M., and Matouschek, A. (2020). A masked initiation region in
658 retinoblastoma protein regulates its proteasomal degradation. Nat Commun *11*, 2019.
659 10.1038/s41467-020-16003-3.

660 45. Wang, Y., Zheng, Z., Zhang, J., Wang, Y., Kong, R., Liu, J., Zhang, Y., Deng, H., Du, X.,
661 and Ke, Y. (2015). A Novel Retinoblastoma Protein (RB) E3 Ubiquitin Ligase (NRBE3)
662 Promotes RB Degradation and Is Transcriptionally Regulated by E2F1 Transcription Factor
663 *. Journal of Biological Chemistry *290*, 28200–28213. 10.1074/jbc.M115.655597.

664 46. Boyer, S.N., Wazer, D.E., and Band, V. (1996). E7 Protein of Human Papilloma Virus-16
665 Induces Degradation of Retinoblastoma Protein through the Ubiquitin-Proteasome
666 Pathway1. Cancer Research *56*, 4620–4624.

667 47. Uchida, C., Miwa, S., Kitagawa, K., Hattori, T., Isobe, T., Otani, S., Oda, T., Sugimura, H.,
668 Kamijo, T., Ookawa, K., et al. (2005). Enhanced Mdm2 activity inhibits pRB function via
669 ubiquitin-dependent degradation. EMBO J *24*, 160–169. 10.1038/sj.emboj.7600486.

670 48. Liu, H., Wang, J., Liu, Y., Hu, L., Zhang, C., Xing, B., and Du, X. (2018). Human U3
671 protein14a is a novel type ubiquitin ligase that binds RB and promotes RB degradation
672 depending on a leucine-rich region. Biochimica et Biophysica Acta (BBA) - Molecular Cell
673 Research *1865*, 1611–1620. 10.1016/j.bbamcr.2018.08.016.

674 49. Sun, E., and Zhang, P. (2021). RNF12 Promotes Glioblastoma Malignant Proliferation via
675 Destructing RB1 and Regulating MAPK Pathway. J Healthc Eng *2021*, 4711232.
676 10.1155/2021/4711232.

677 50. de Vivo, A., Sanchez, A., Yegres, J., Kim, J., Emly, S., and Kee, Y. (2019). The OTUD5–
678 UBR5 complex regulates FACT-mediated transcription at damaged chromatin. Nucleic
679 Acids Research *47*, 729–746. 10.1093/nar/gky1219.

680 51. Gudjonsson, T., Altmeyer, M., Savic, V., Toledo, L., Dinant, C., Grøfte, M., Bartkova, J.,
681 Poulsen, M., Oka, Y., Bekker-Jensen, S., et al. (2012). TRIP12 and UBR5 Suppress
682 Spreading of Chromatin Ubiquitylation at Damaged Chromosomes. Cell *150*, 697–709.
683 10.1016/j.cell.2012.06.039.

52. Tsai, J.M., Aguirre, J.D., Li, Y.-D., Brown, J., Focht, V., Kater, L., Kempf, G., Sandoval, B., Schmitt, S., Rutter, J.C., et al. (2023). UBR5 forms ligand-dependent complexes on chromatin to regulate nuclear hormone receptor stability. Molecular Cell *0*. 10.1016/j.molcel.2023.06.028.

53. Mark, K.G., Kolla, S., Aguirre, J.D., Garshott, D.M., Schmitt, S., Haakonsen, D.L., Xu, C., Kater, L., Kempf, G., Martínez-González, B., et al. (2023). Orphan quality control shapes network dynamics and gene expression. Cell *0*. 10.1016/j.cell.2023.06.015.

54. Azuma, H., Paulk, N., Ranade, A., Dorrell, C., Al-Dhalimy, M., Ellis, E., Strom, S., Kay, M.A., Finegold, M., and Grompe, M. (2007). Robust expansion of human hepatocytes in Fah-/-/Rag2-/-/Il2rg-/- mice. Nat Biotechnol *25*, 903–910. 10.1038/nbt1326.

55. Grompe, M. (2017). Fah Knockout Animals as Models for Therapeutic Liver Repopulation. Adv Exp Med Biol *959*, 215–230. 10.1007/978-3-319-55780-9_20.

56. Zhu, M., Lu, T., Jia, Y., Luo, X., Gopal, P., Li, L., Odewole, M., Renteria, V., Singal, A.G., Jang, Y., et al. (2019). Somatic Mutations Increase Hepatic Clonal Fitness and Regeneration in Chronic Liver Disease. Cell *177*, 608-621.e12. 10.1016/j.cell.2019.03.026.

57. Curtis, C., Shah, S.P., Chin, S.-F., Turashvili, G., Rueda, O.M., Dunning, M.J., Speed, D., Lynch, A.G., Samarajiwa, S., Yuan, Y., et al. (2012). The genomic and transcriptomic architecture of 2,000 breast tumours reveals novel subgroups. Nature *486*, 346–352. 10.1038/nature10983.

58. Rueda, O.M., Sammut, S.-J., Seoane, J.A., Chin, S.-F., Caswell-Jin, J.L., Callari, M., Batra, R., Pereira, B., Bruna, A., Ali, H.R., et al. (2019). Dynamics of breast-cancer relapse reveal late-recurring ER-positive genomic subgroups. Nature *567*, 399–404. 10.1038/s41586-019-1007-8.

59. Hehl, L.A., Horn-Ghetko, D., Prabu, J.R., Vollrath, R., Vu, D.T., Berrocal, D.A.P., Mulder, M.P.C., Noort, G.J. van der H. van, and Schulman, B.A. (2023). Structural snapshots along K48-linked ubiquitin chain formation by the HECT E3 UBR5. Preprint at bioRxiv, 10.1101/2023.06.06.543850 10.1101/2023.06.06.543850.

60. Hodáková, Z., Grishkovskaya, I., Brunner, H.L., Bolhuis, D.L., Belačić, K., Schleiffer, A., Kotisch, H., Brown, N.G., and Haselbach, D. (2022). Cryo-EM structure of the chain-elongating E3 ligase UBR5. Preprint at bioRxiv, 10.1101/2022.11.03.515015 10.1101/2022.11.03.515015.

61. Wang, F., He, Q., Zhan, W., Yu, Z., Finkin-Groner, E., Ma, X., Lin, G., and Li, H. (2023). Structure of the human UBR5 E3 ubiquitin ligase. Structure *31*, 541-552.e4. 10.1016/j.str.2023.03.010.

62. Jiang, W., Wang, S., Xiao, M., Lin, Y., Zhou, L., Lei, Q., Xiong, Y., Guan, K.-L., and Zhao, S. (2011). Acetylation regulates gluconeogenesis by promoting PEPCK1 degradation via recruiting the UBR5 ubiquitin ligase. Mol Cell *43*, 33–44. 10.1016/j.molcel.2011.04.028.

63. Sanidas, I., Lee, H., Rumde, P.H., Boulay, G., Morris, R., Golczer, G., Stanzione, M., Hajizadeh, S., Zhong, J., Ryan, M.B., et al. (2022). Chromatin-bound RB targets promoters,

723 enhancers, and CTCF-bound loci and is redistributed by cell-cycle progression. Mol Cell *82*,
724 3333-3349.e9. 10.1016/j.molcel.2022.07.014.

725 64. Suski, J.M., Braun, M., Strmiska, V., and Sicinski, P. (2021). Targeting cell-cycle machinery
726 in cancer. Cancer Cell *39*, 759–778. 10.1016/j.ccell.2021.03.010.

727 65. Finn, R.S., Martin, M., Rugo, H.S., Jones, S., Im, S.-A., Gelmon, K., Harbeck, N., Lipatov,
728 O.N., Walshe, J.M., Moulder, S., et al. (2016). Palbociclib and Letrozole in Advanced Breast
729 Cancer. New England Journal of Medicine *375*, 1925–1936. 10.1056/NEJMoa1607303.

730 66. Hortobagyi, G.N., Stemmer, S.M., Burris, H.A., Yap, Y.-S., Sonke, G.S., Paluch-Shimon, S.,
731 Campone, M., Blackwell, K.L., André, F., Winer, E.P., et al. (2016). Ribociclib as First-Line
732 Therapy for HR-Positive, Advanced Breast Cancer. N Engl J Med *375*, 1738–1748.
733 10.1056/NEJMoa1609709.

734 67. Sherr, C.J., Beach, D., and Shapiro, G.I. (2016). Targeting CDK4 and CDK6: From
735 Discovery to Therapy. Cancer Discovery *6*, 353–367. 10.1158/2159-8290.CD-15-0894.

736 68. Garrido-Castro, A.C., and Goel, S. (2017). CDK4/6 Inhibition in Breast Cancer: Mechanisms
737 of Response and Treatment Failure. Curr Breast Cancer Rep *9*, 26–33. 10.1007/s12609-
738 017-0232-0.

739 69. Spring, L.M., Wander, S.A., Andre, F., Moy, B., Turner, N.C., and Bardia, A. (2020). Cyclin-
740 dependent kinase 4 and 6 inhibitors for hormone receptor-positive breast cancer: past,
741 present, and future. The Lancet *395*, 817–827. 10.1016/S0140-6736(20)30165-3.

742 70. Malumbres, M., Sotillo, R., Santamaría, D., Galán, J., Cerezo, A., Ortega, S., Dubus, P.,
743 and Barbacid, M. (2004). Mammalian cells cycle without the D-type cyclin-dependent
744 kinases Cdk4 and Cdk6. Cell *118*, 493–504. 10.1016/j.cell.2004.08.002.

745 71. Kozar, K., Ciemerych, M.A., Rebel, V.I., Shigematsu, H., Zagozdzon, A., Sicinska, E., Geng,
746 Y., Yu, Q., Bhattacharya, S., Bronson, R.T., et al. (2004). Mouse development and cell
747 proliferation in the absence of D-cyclins. Cell *118*, 477–491. 10.1016/j.cell.2004.07.025.

748 72. Regev, A., Teichmann, S.A., Lander, E.S., Amit, I., Benoist, C., Birney, E., Bodenmiller, B.,
749 Campbell, P., Carninci, P., Clatworthy, M., et al. (2017). The Human Cell Atlas. eLife *6*,
750 e27041. 10.7554/eLife.27041.

751 73. Abraham, K.J., Khosraviani, N., Chan, J.N.Y., Gorthi, A., Samman, A., Zhao, D.Y., Wang,
752 M., Bokros, M., Vidya, E., Ostrowski, L.A., et al. (2020). Nucleolar RNA polymerase II drives
753 ribosome biogenesis. Nature *585*, 298–302. 10.1038/s41586-020-2497-0.

754 74. Charni-Natan, M., and Goldstein, I. (2020). Protocol for Primary Mouse Hepatocyte
755 Isolation. STAR Protoc *1*, 100086. 10.1016/j.xpro.2020.100086.

756 75. Jin, Y., Anbarchian, T., Wu, P., Sarkar, A., Fish, M., Peng, W.C., and Nusse, R. (2022). Wnt
757 signaling regulates hepatocyte cell division by a transcriptional repressor cascade.
758 Proceedings of the National Academy of Sciences *119*, e2203849119.
759 10.1073/pnas.2203849119.

760 76. Berenson, D.F., Zatulovskiy, E., Xie, S., and Skotheim, J.M. (2019). Constitutive expression
761 of a fluorescent protein reports the size of live human cells. MBoC *30*, 2985–2995.
762 10.1091/mbc.E19-03-0171.

763 77. Lucchesi, C., Mohibi, S., and Chen, X. (2021). Measuring Translation Efficiency by RNA
764 Immunoprecipitation of Translation Initiation Factors. Methods Mol Biol *2267*, 73–79.
765 10.1007/978-1-0716-1217-0_5.

766 78. Liu, X., Yan, J., and Kirschner, M.W. (2022). Beyond G1/S regulation: how cell size
767 homeostasis is tightly controlled throughout the cell cycle? Preprint at bioRxiv,
768 10.1101/2022.02.03.478996 10.1101/2022.02.03.478996.

769 79. Pereira, B., Chin, S.-F., Rueda, O.M., Vollan, H.-K.M., Provenzano, E., Bardwell, H.A.,
770 Pugh, M., Jones, L., Russell, R., Sammut, S.-J., et al. (2016). The somatic mutation profiles
771 of 2,433 breast cancers refine their genomic and transcriptomic landscapes. Nat Commun
772 *7*, 11479. 10.1038/ncomms11479.

773
774
775

Acknowledgements
We thank Julien Sage, Seth Rubin, Hao Zhu, Peter Pryciak and members of the Skotheim laboratory for discussions and feedback on the manuscript. We thank Hao Zhu for sharing the *Fah* transposon plasmids. We thank Markus Grompe for sharing the *Fah-/-* mice. This work was supported by a Chan Zuckerberg Biohub Investigator Award (J.M.S.), and the NIH (P01 CA254867 and K99GM147351). The siRNA screens were done using the ImageXpress Micro CONFOCAL microscope at the High Throughput Screening Knowledge Center (HTSKC) at Stanford, which was funded by the NIH Shared Instrumentation Grant (S10OD026899).

Author contributions
S.Z. performed the experiments, L.V. performed the mathematical modeling, E.Z., S.Z, and J.M.S. designed the experiments, L.M. and C.C performed the cancer genomics analysis, and S.Z. and J.M.S. wrote the manuscript.

Competing interests
The authors declare no competing interest.

Figures and Figure captions

Figure 1

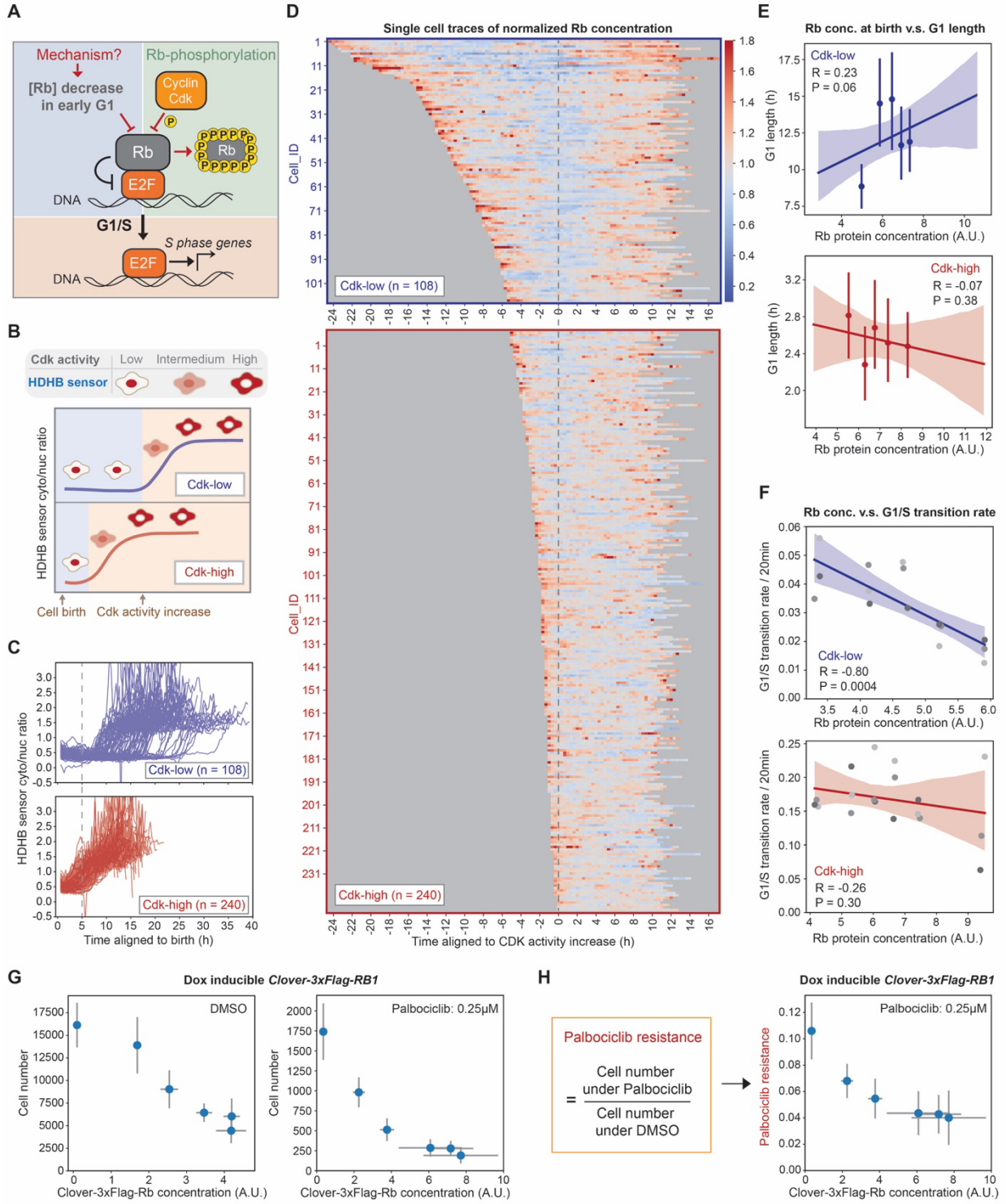

802 **Figure 1. Rb concentration dynamics regulate cell cycle progression in Cdk-low cells**
803 **A.** Schematic illustration of two parallel pathway acting through Rb concentration and Rb
804 phosphorylation to promote the G1/S transition. **B**. Schematic illustration of the Cdk activities in
805 Cdk-low and Cdk-high categories of cells. Cdk activity is measured using the HDHB sensor
806 whose translocation to the cytoplasm from the nucleus is driven by Cdk activity. Cdk activation
807 is defined using the inflection point in the cytoplasm-to-nuclear ratio. **C.** Fluorescent traces
808 showing the HDHB cytoplasm-to-nucleus intensity ratio from HMEC-hTERT1 cells expressing
809 endogenously tagged *RB1-3xFLAG-Clover-sfGFP* and the HDHB Cdk sensor [25]. Cdk-high cells
810 are defined as those activating Cdk within 5 hours of their birth, while Cdk-low cells activate Cdk
811 later. **D.** Individual fluorescent traces from the cells in (C). Upper panel shows Cdk-low cells,
812 and the lower panel shows Cdk-high cells. Traces are aligned by the initial translocation of the
813 HDHB Cdk sensor. The trace color represents the normalized Rb protein concentration
814 (normalized to the mean Rb concentration of the cells in the same group). **E**. The correlations
815 between Rb concentration at birth and G1 length in Cdk-low and Cdk-high cells. **F**. The
816 correlations between Rb concentration and G1/S transition rate in Cdk-low and Cdk-high cells.
817 **G.** Cell number of HMEC cells treated with 0.25 μM Palbociclib for 72 hours. Cells were plated
818 in different doses of doxycycline to induce exogenous Clover-3xFlag-Rb. Drug treatment started
819 the next day and lasted for 72 hours. Then, cells were fixed and the cell number in each well
820 was measured. **H**. Normalized cell number of the cells treated as described in panel (**G**).
821 Normalized cell number is the cell number following Palbociclib treatment divided by the cell
822 number under DMSO control treatment. n = 3 biological replicates, the error bars indicate
823 standard deviation.
824

825 **Figure 2**
826

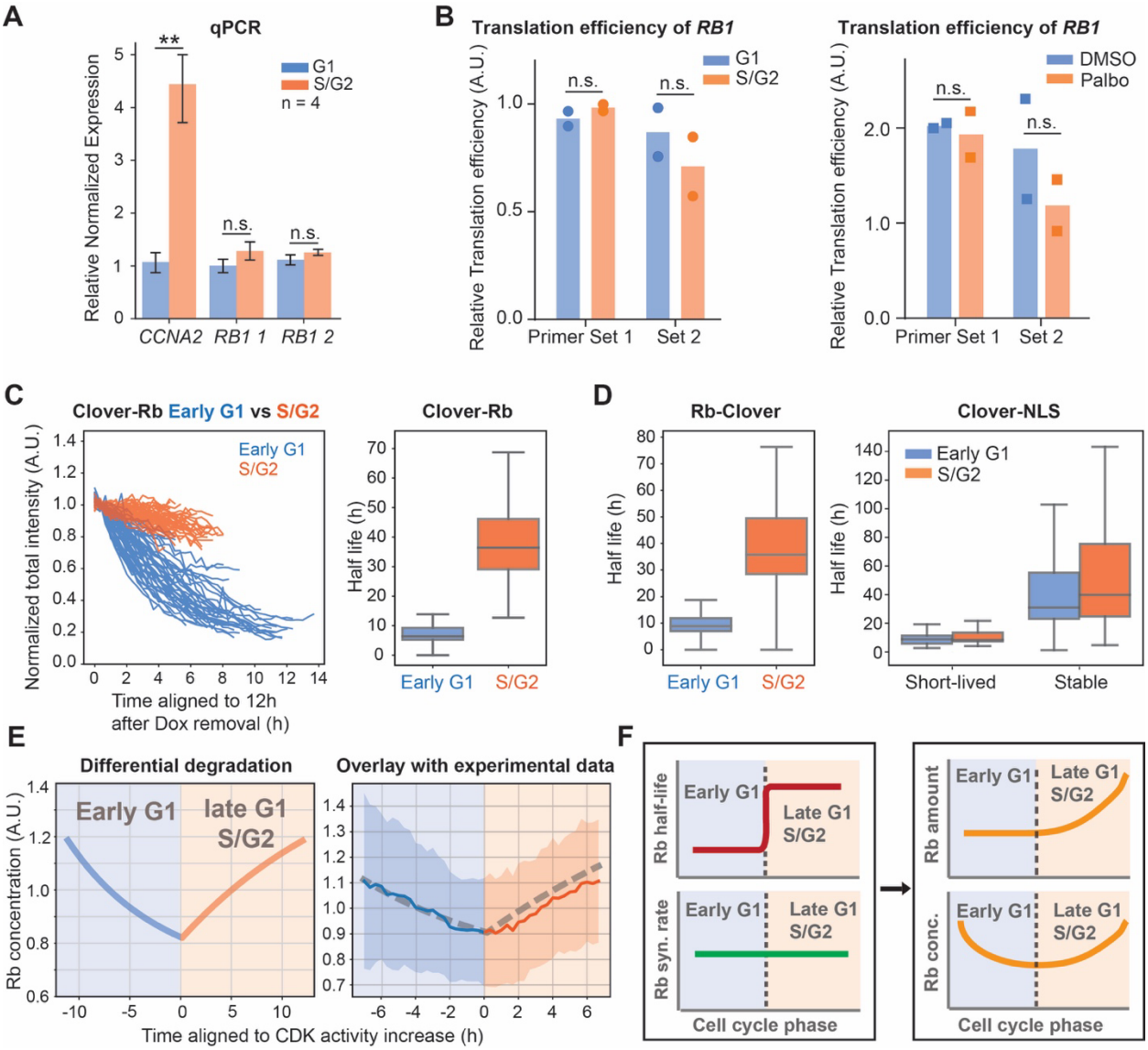

827
828

829 **Figure 2. Rb concentration dynamics are driven by cell cycle-dependent protein**
830 **degradation**
831 **A.** qPCR (n = 4) measurements of the *RB1* mRNA concentration in G1 and S/G2 HMEC cells
832 sorted using a FUCCI cell cycle reporter. **B**. Translation efficiency (TE) of *RB1* was determined
833 in HMEC cells in G1 and S/G2 that had been sorted using a FUCCI marker (left panel), and in
834 HMEC cells treated with DMSO or Palbociclib (1μM) (right panel). TE was measured using a
835 RIP assay (RNA binding protein immunoprecipitation) by pulling down eIF4E. TE is calculated
836 by dividing the eIF4E bound fraction of *RB1* mRNA to the eIF4E bound fraction of *GAPDH* and
837 *Actin* mRNAs. Bars denote mean values and dots denote each replicate experiment. **C.** (Left
838 panel) The degradation traces of Clover-3xFlag-Rb protein after Dox withdrawal. The traces
839 were classified into early G1 phase or S/G2 phase based on a FUCCI cell cycle marker and cell
840 cycle phase duration. (Right panel) Distribution of half-lives estimated from exponential fits. Box
841 plot indicates 5th, 25th, median, 75th and 95th percentiles. **D.** Same half-life measurement as in
842 panel (**C**), but using a C-terminally tagged Rb-3xFlag-Clover (Left panel), a short-lived Clover-
843 NLS, and a stable Clover-NLS (Right panel). **E**. Left panel: Rb concentration dynamics
844 assuming that its degradation rate decreases by 80% at the G1/S transition as measured by live
845 imaging (see Figure 2C) and its synthesis rate does not change (left panel). Right panel shows
846 the overlay of the model based on regulated Rb degradation with the experimental data from
847 Figure S1D (Cdk-low cells). Rb concentration is normalized to the mean. **F.** Model schematic:
848 differential degradation of Rb in G1 and S/G2 phases of the cell cycle drive its concentration
849 dynamics.
850
851

852 **Figure 3**
853

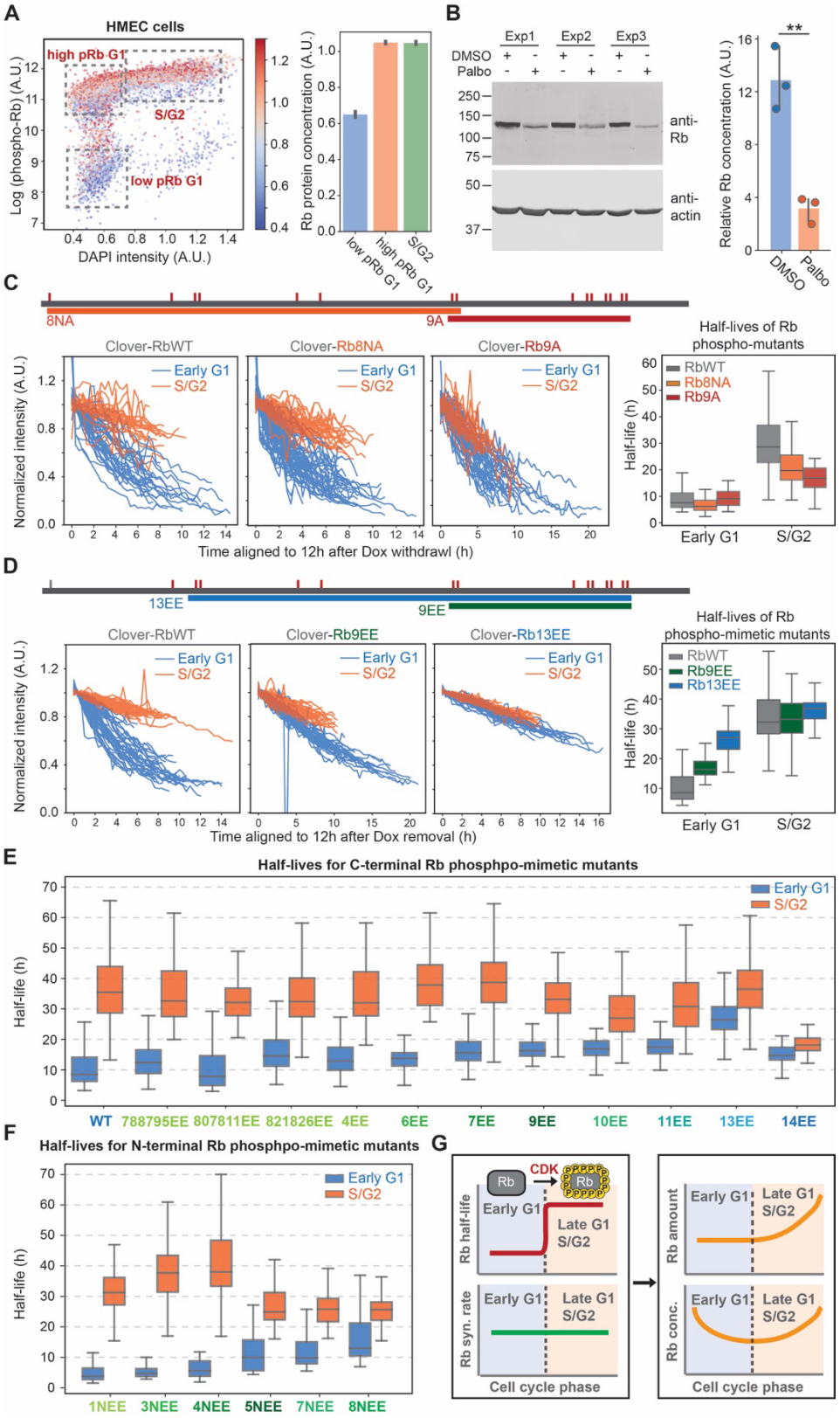

854
855

856 **Figure 3. Rb protein is stabilized via phosphorylation by Cyclin-Cdk**
857 **A.** Rb concentration in different phospho-Rb populations. HMEC cells were stained with
858 phospho-Rb (S807/811) and Rb antibodies. (Left panel) phospho-Rb intensity is plotted against
859 DNA content (DAPI intensity). The color indicates Rb concentration. (Right panel) quantification
860 of Rb concentrations in different phospho-Rb populations gated using the indicated boxes in the
861 left panel. Bar plots indicate the mean and 95% confidence interval. **B.** Immunoblot of Rb after
862 DMSO or Palbociclib (1μM) treatment for 24 hours. The quantification of relative Rb
863 concentration (normalized to actin intensity) is shown on the right. **C.** Top panel shows the
864 schematic of Rb phospho-site mutants. Small red lines indicate the location of Cdk
865 phosphorylation sites. Lower panel shows the degradation traces for Clover-3xFlag-RbWT,
866 Clover-3xFlag-Rb8NA, and Clover-3xFlag-Rb9A as well as the corresponding distributions of
867 half-lives. **D.** Top panel shows the schematic of the Rb phospho-mimetic mutants. Lower panel
868 shows the degradation traces for Clover-3xFlag-RbWT, Clover-3xFlag-Rb9EE, and Clover-
869 3xFlag-Rb13EE, as well as the corresponding distributions of half-lives. **E-F.** Half-life
870 distributions for all the Rb phospho-mimetic mutants. **G.** Model schematic: Rb is stabilized in
871 late G1 and S/G2 phases by Cdk phosphorylation.
872

873 **Figure 4**
874

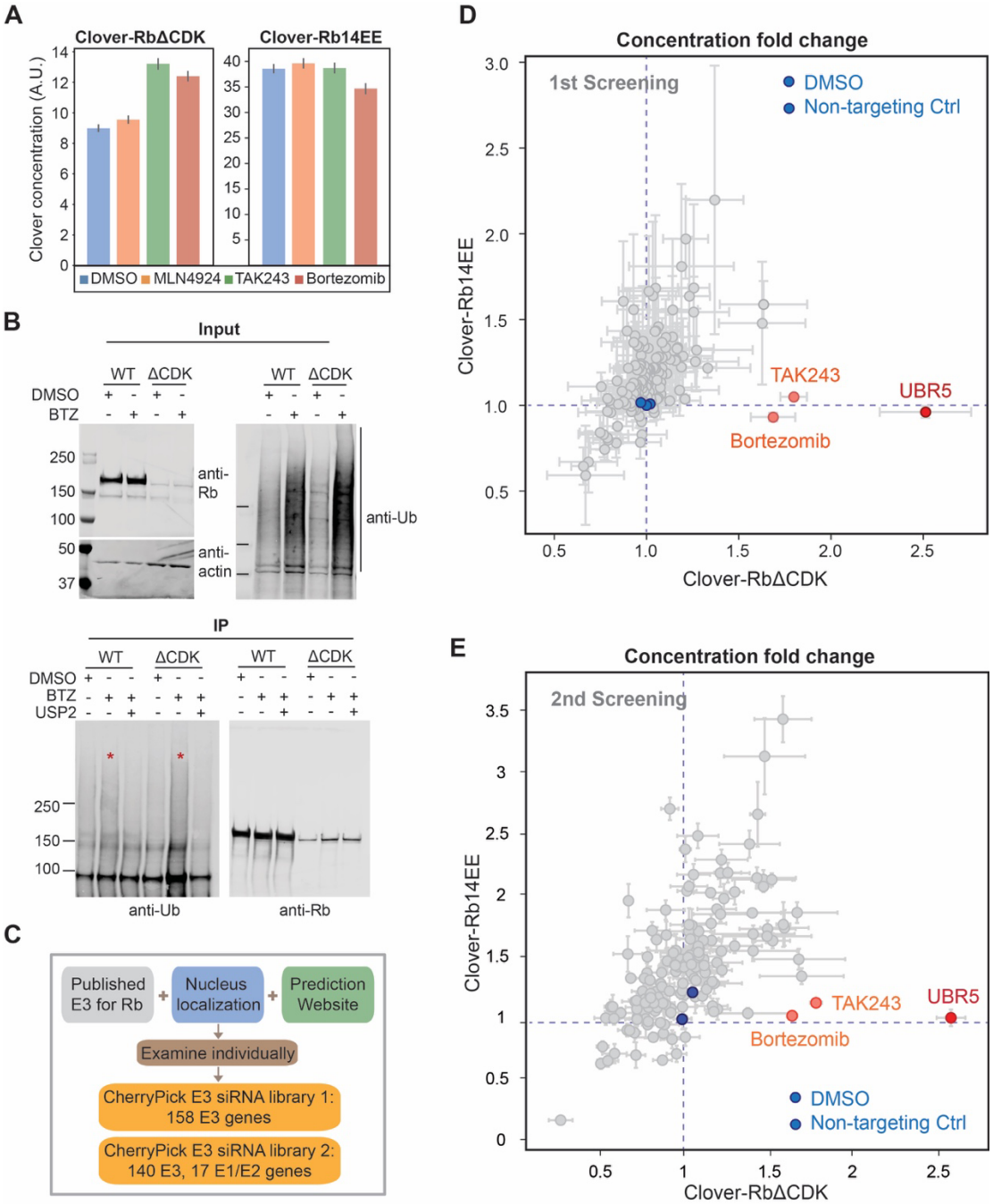

875
876
877

878 **Figure 4. siRNA screens identified UBR5 as the E3 ligase targeting un-phosphorylated Rb**
879 **for degradation**
880 **A.** Concentrations of Clover-3xFlag-RbΔCDK or Clover-3xFlag-Rb14EE after drug treatments.
881 Cells expressing Clover-3xFlag-RbΔCDK and Clover-3xFlag-Rb14EE were induced with Dox
882 (1μg/mL) for 48 hours. Then, cells were treated with the indicated drugs for 5 hours, fixed, and
883 imaged. The concentrations of Clover-3xFlag-Rb variants were calculated by dividing total
884 Clover intensity by nuclear area$^{3/2}$. **B**. Un-phosphorylated Rb is degraded via ubiquitination.
885 HMEC cells expressing Clover-3xFlag-RbΔCDK or RbWT (induced by 1μg/ml Dox for 48 hours)
886 were treated with Bortezomib (1μM) or DMSO for 5 hours before collection. Clover-3xFlag-
887 RbΔCDK or RbWT proteins were immunoprecipitated using anti-Flag magnetic beads. After
888 purification, the Bortezomib treated samples were split in half and one half underwent a
889 deubiquitination assay using USP2. The samples were then detected for Rb and Ubiquitin using
890 immunoblot. **C.** Schematics showing siRNA library components. **D-E.** Results of the 1st and 2nd
891 siRNA screens. The concentration fold changes of Clover-3xFlag-RbΔCDK and Clover-3xFlag-
892 Rb14EE are plotted. The fold change is calculated by dividing the Clover concentration of the
893 treatment well by the concentration of the non-treated well. n = 4 biological replicates for the first
894 screen and n = 3 biological replicates for the second screen.
895

Figure 5

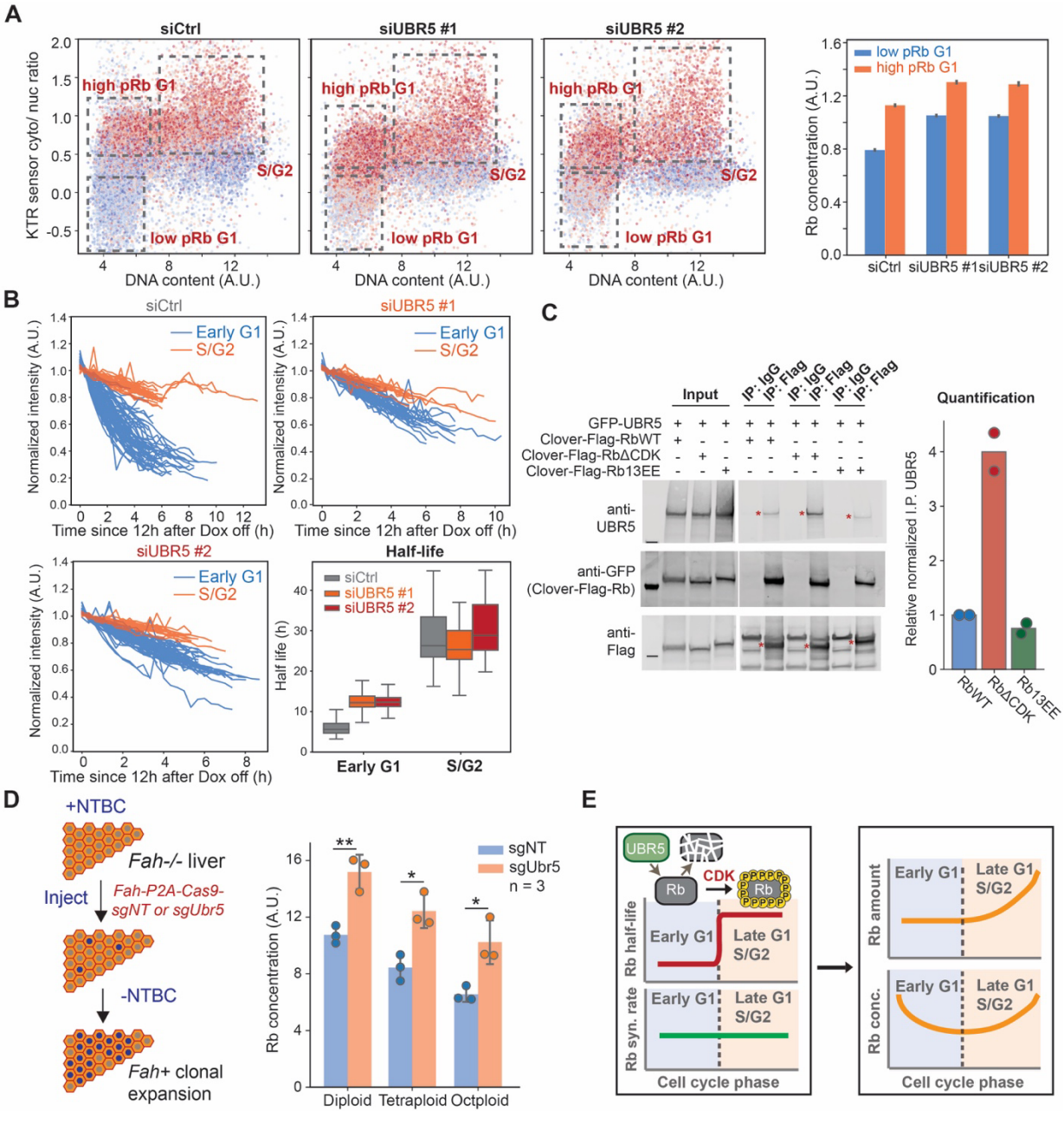
A
siCtrl
siUBR5 #1
siUBR5 #2
KTR sensor cyto/ nuc ratio
high pRb G1
S/G2
low pRb G1
DNA content (A.U.)
Rb concentration (A.U.)
low pRb G1
high pRb G1
siCtrl
siUBR5 #1
siUBR5 #2
B
Normalized intensity (A.U.)
Early G1
S/G2
Time since 12h after Dox off (h)
Half-life
Half life (h)
Early G1
S/G2
C
Input
IP: IgG
IP: Flag
GFP-UBR5
Clover-Flag-RbWT
Clover-Flag-RbΔCDK
Clover-Flag-Rb13EE
anti-UBR5
anti-GFP (Clover-Flag-Rb)
anti-Flag
Quantification
Relative normalized I.P. UBR5
RbWT
RbΔCDK
Rb13EE
D
+NTBC
Fah-/- liver
Inject
Fah-P2A-Cas9-sgNT or sgUbr5
-NTBC
Fah+ clonal expansion
Rb concentration (A.U.)
sgNT
sgUbr5
n = 3
Diploid
Tetraploid
Octploid
E
UBR5
Rb
CDK
Rb half-life
Rb syn. rate
Early G1
Late G1
S/G2
Cell cycle phase
Rb amount
Rb conc.

900 **Figure 5. Validation of UBR5 as the E3 ligase mediating the degradation of un-**
901 **phosphorylated Rb**
902 **A.** Microscopy analysis of HMEC cells expressing the Rb (886-928) KTR sensor [36], which
903 reflects Cdk activity. Cells were treated with Ctrl siRNA or *UBR5* siRNAs for 48 hours. The
904 cytoplasmic-to-nucleus intensity ratio of the KTR sensor is plotted against DNA content (DAPI
905 staining). The dot color indicates the Rb concentration. Quantification of the Rb concentration
906 for different phospho-Rb levels is shown on the right. Bars indicate mean and the 95%
907 confidence interval. **B.** Degradation traces and the calculated half-lives of Clover-3xFlag-Rb
908 after *UBR5* knock down. Box plot indicates 5th, 25th, median, 75th and 95th percentiles. **C.** Un-
909 phosphorylated Rb interacts with the E3 ligase UBR5. HEK293 cells were transfected with a
910 Clover-3xFlag-RbWT, RbΔCDK, or Rb13EE construct as well as a GFP-UBR5 construct
911 (addgene #52050). 24 hours after transfection, cells were induced by Dox. After 24 hours of
912 induction, cells were lysed, and Flag antibodies were used to pull down Clover-3xFlag-Rb
913 mutants. The samples were then detected for UBR5 and Rb using immunoblot. For
914 quantification, the co-immunoprecipitated UBR5 was normalized to the immunoprecipitated Rb
915 mutant protein amount and the input UBR5 protein amount. **D.** (Left panel) Schematic of the
916 *Fah-/-* mouse liver model. (Right panel) Rb concentration in the low-phospho-Rb population of
917 the primary hepatocytes isolated from mice receiving *Fah-P2A-Cas9-sgNT* or *Fah-P2A-Cas9-*
918 *sgUbr5* transposons. The error bars indicate the standard deviation of the mean. **E.** Model
919 schematic: Un-phosphorylated Rb is targeted for degradation by the E3 ligase UBR5 in early
920 G1.
921

922 **Figure 6**
923

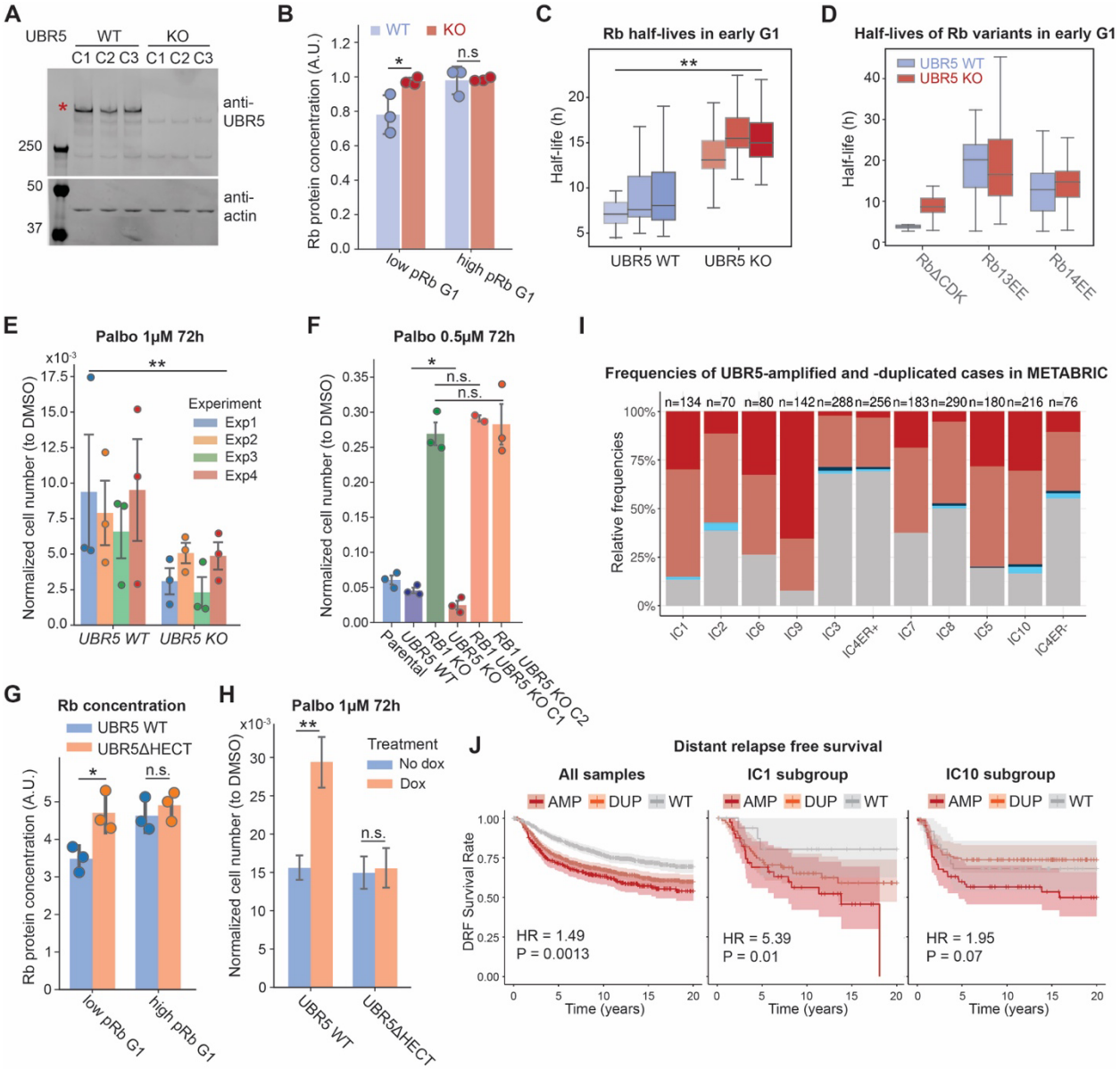

924
925

Figure 6. UBR5 deletion stabilizes Rb and sensitizes cells to CDK4/6 inhibition

A. Immunoblot verification of *UBR5 KO* clonal cell lines. **B.** Quantification of Rb concentration in different phospho-Rb populations of *UBR5 WT* or *KO* clonal cell lines expressing the Rb (886-928) KTR sensor [36]. Circles denote results from individual clones and the bars denote the standard deviation. **C.** The half-life distributions of Clover-3xFlag-RbWT protein in early G1 phase from 6 clonal cell lines (3 *WT*, 3 *UBR5 KO*). **D.** The half-life distributions of Clover-3xFlag-RbΔCDK, Rb13EE, and Rb14EE in early G1 phase in *UBR5 WT* and *UBR5 KO* cells. **E.** Normalized cell number of *UBR5 WT* and *KO* clonal cell lines after Palbociclib (1μM) treatment for 72 hours. Drug treatment started the day after plating. After 72 hours of drug treatment, cells were fixed and the cell number in each well was measured. Normalized cell number is the cell number following a Palbociclib treatment divided by the cell number following a DMSO control treatment. n = 4 biological replicates and error bars indicate the standard deviation. **F.** Normalized cell number for *UBR5 WT*, *RB1 KO*, and *RB1 UBR5* double *KO* clonal cell lines following Palbociclib (0.5μM) treatment for 72 hours. n = 3 biological replicates. **G.** Quantification of Rb concentration in different phospho-Rb populations of *UBR5 KO* cells with either *UBR5 WT* or *UBR5ΔHECT* added back by Dox-induction. Circles denote results from individual clones and the bars denote the standard deviation. **H.** Normalized cell number of *UBR5 KO* cells with *UBR5 WT* or *UBR5ΔHECT* added back following Palbociclib (1μM) treatment for 72 hours. GFP-UBR5 WT or GFP-UBR5ΔHECT were induced by Dox (100ng/ml). The results show the average from 3 *UBR5 KO* clonal cell lines with different UBR5 variants added back. We performed 3 biological replicates. The error bars indicate the standard deviation. **I.** Frequencies of *UBR5*-amplification and *UBR5*-duplication in the METABRIC dataset across the different breast cancer subtypes and IC subgroups. The number of tumors within each group is indicated on the top of each bar. AMP = amplification corresponding to a total copy number ≥ 6; DUP = duplication corresponding to a total copy number between 3 and 5; Hetero_DEL = heterozygous deletion; nLOH = neutral loss-of-heterozygosity. **J.** Kaplan-Meier curves of distant relapse-free (DRF) survival for the *UBR5*-amplified, *UBR5*-duplicated, and WT cases across all samples (left panel), in the IC1 subgroup (middle panel), and in the IC10 subgroup (right panel). The squares correspond to estimated hazard ratios and the segments correspond to their 95% confidence intervals. HR = hazard ratio. P-value tests the difference between the WT and the AMP curves corrected for the other clinical covariates. Survival analysis was performed using Cox's proportional hazard models, comparing *UBR5*-amplified to WT cases and corrected for the clinical covariates (age, grade, tumor size, lymph node, and ER status) [58].

962 **Figure 7**
963

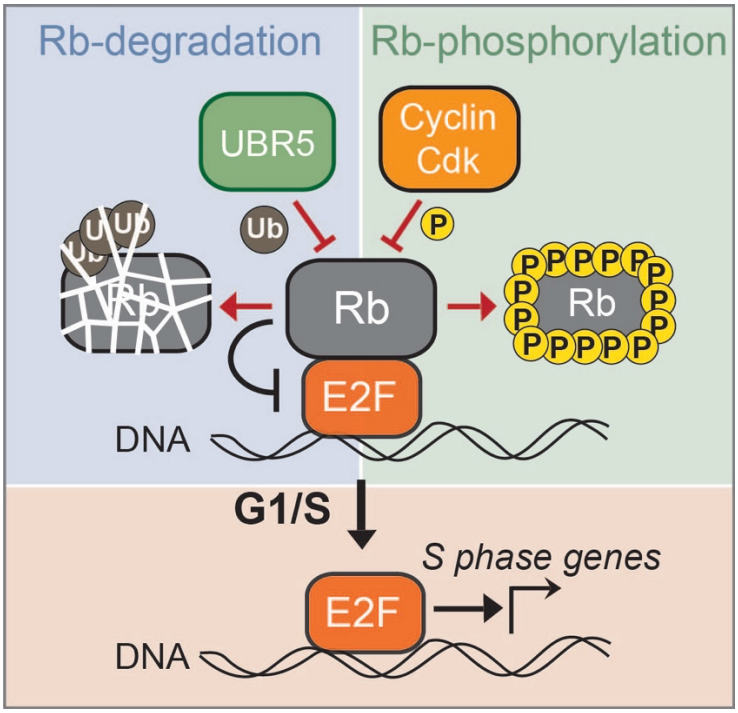

964
965
966 **Figure 7**. Model schematic of parallel pathways regulating Rb activity and thereby the G1/S
967 transition. Rb is targeted for degradation by UBR5 in parallel to the canonical Rb phosphorylation
968 pathway.
969
970

Figure S1

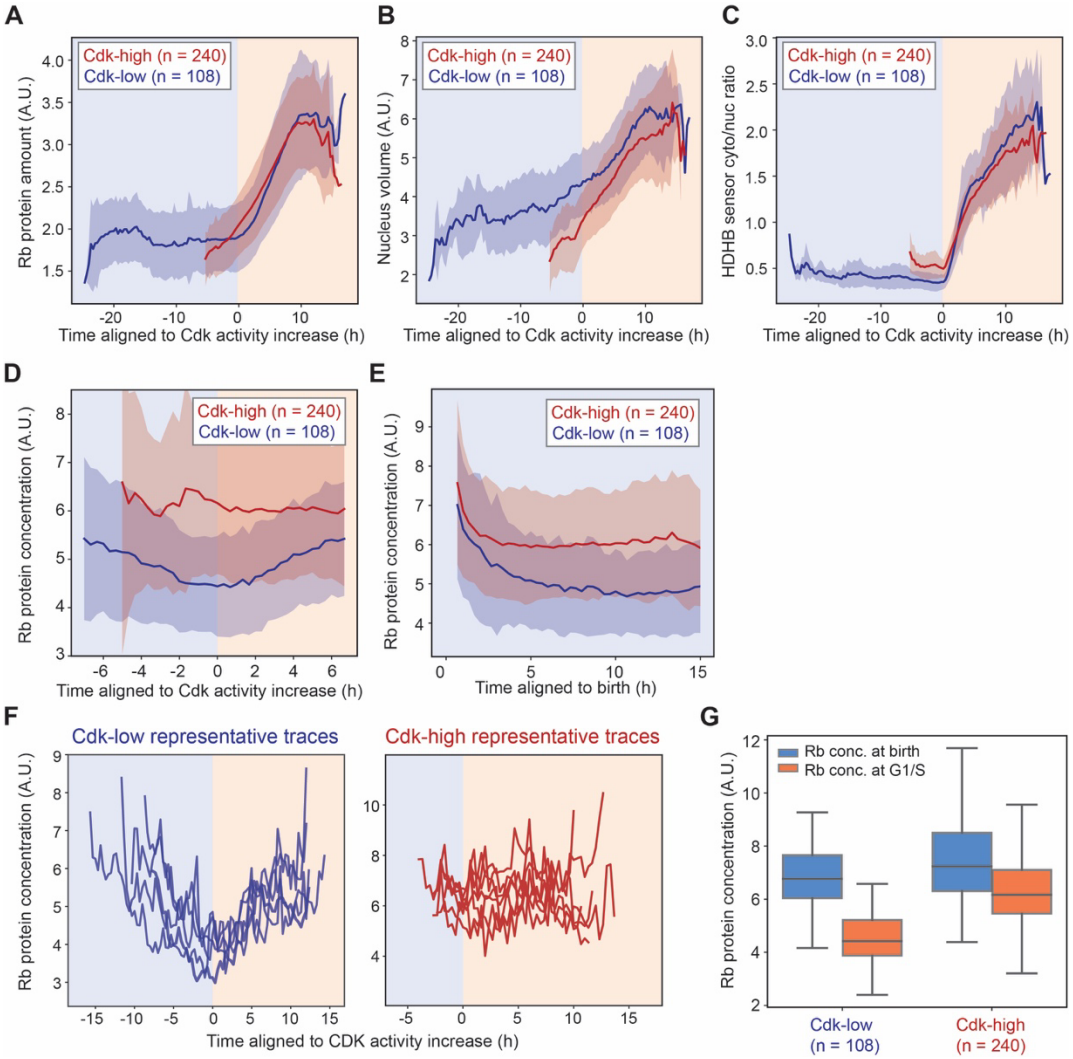
A
Cdk-high (n = 240)
Cdk-low (n = 108)
Rb protein amount (A.U.)
Time aligned to Cdk activity increase (h)
B
Nucleus volume (A.U.)
C
HDHB sensor cyto/nuc ratio
D
Rb protein concentration (A.U.)
E
Time aligned to birth (h)
F
Cdk-low representative traces
Cdk-high representative traces
Time aligned to CDK activity increase (h)
G
Rb conc. at birth
Rb conc. at G1/S
Cdk-low (n = 108)
Cdk-high (n = 240)

Figure S1. Rb concentration continuously decreases in early G1 phase in Cdk-low cells. **A-E.** Live-cell imaging of HMEC-hTERT1 cells expressing endogenously tagged *RB1-3xFLAG-Clover-sfGFP* and the HDHB CDK sensor [1]. Cdk-high and Cdk-low cells were grouped as in Fig. 1C. Average traces for the total amount of Rb-3xFLAG-Clover-sfGFP protein (A), nuclear volume (B), the cytoplasmic-to-nuclear intensity ratio of the HDHB sensor (C), and the protein concentration of Rb-3xFLAG-Clover-sfGFP (D, E) are plotted. Traces are aligned by the inflection point of the cytoplasm-to-nuclear ratio of the HDHB sensor, which indicates the initial rise of CDK activity (A-C), or aligned at birth (E). Shaded region denotes the standard deviation. **F**. Representative single cell traces showing the Rb concentration dynamics of Cdk-low and Cdk-high cells. Cells were aligned to the G1/S transition. **G**. Comparing Rb concentrations at birth or at the G1/S transition (Cdk activation point) in Cdk-low and Cdk-high cells.

989 **Figure S2**
990

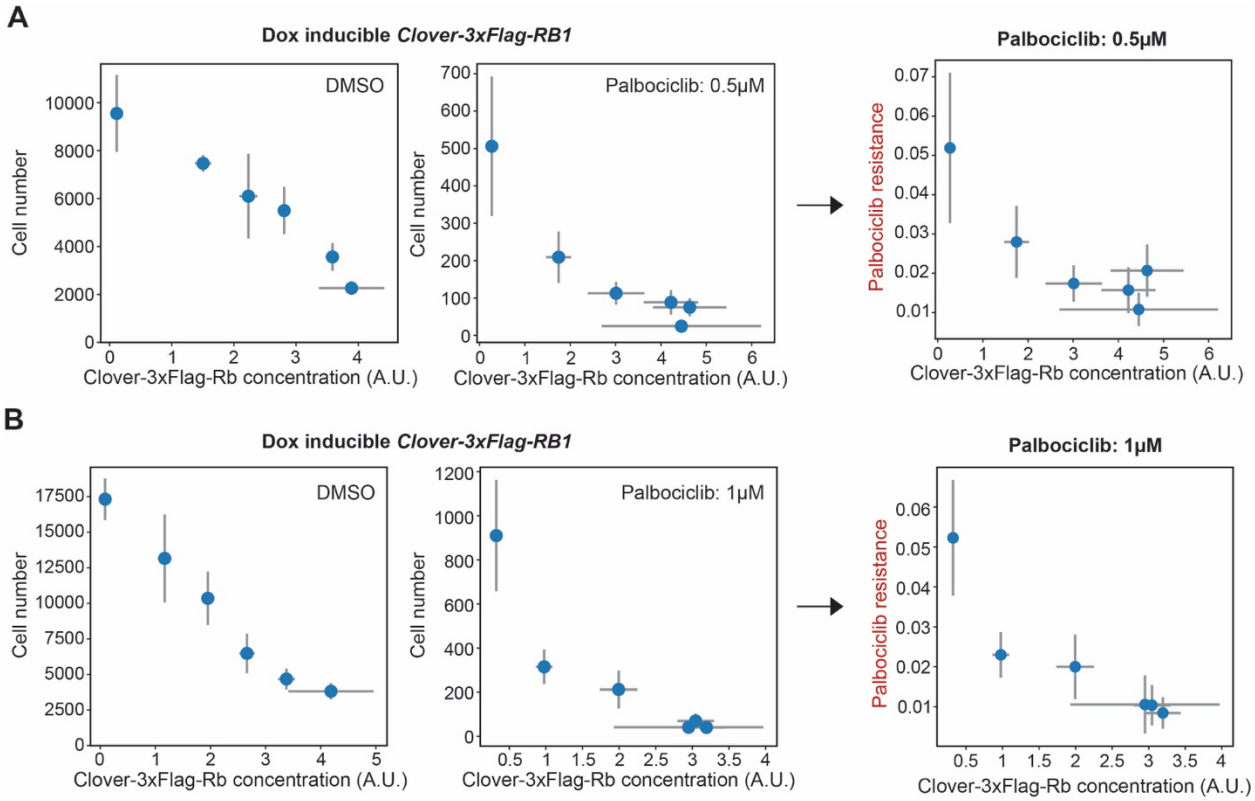

991
992
993
994 **Figure S2. Rb overexpression increases the sensitivity of cells to CDK4/6 inhibition**
995 **A-B.** Cell number and normalized cell number of HMEC cells treated with 0.5μM (A) or 1μM (B)
996 Palbociclib for 72 hours. Cells were plated in different doses of doxycycline to induce
997 exogenous Clover-3xFlag-Rb. Drug treatment started the next day and lasted for 72 hours.
998 Then, cells were fixed and the cell number in each well was measured. Normalized cell number
999 is the cell number under Palbociclib treatment divided by the cell number under DMSO
1000 treatment. N = 3 biological replicates and the error bars indicate standard deviations.
1001

1002 **Figure S3**

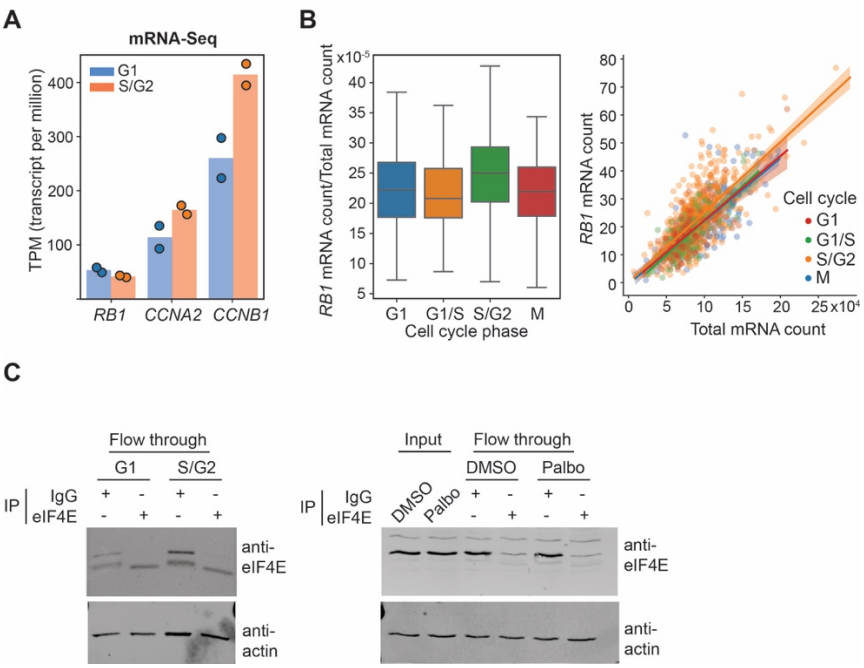

1003
1004
1005
1006 **Figure S3. The synthesis rate of *RB1* is relatively constant through the cell cycle.**
1007 **A.** mRNA-Seq (n = 2) measurements for *RB1* mRNA concentration in G1 and S/G2 HMEC cells
1008 sorted using a FUCCI marker. **B.** Analysis of published MERFISH data[35] for *RB1* mRNA
1009 concentrations. (Left panel) the *RB1* mRNA concentration in different cell cycle phases
1010 classified using the cell cycle dependent genes identified from the paper. *RB1* mRNA
1011 concentration is calculated by dividing the *RB1* mRNA count by the total mRNA count. (Right
1012 panel) mRNA count of *RB1* is proportional to the total mRNA count in different cell cycle
1013 phases. **C.** Western blot of eIF4E. RIP (RNA binding protein immunoprecipitation) assay for
1014 pulling down eIF4E was performed on G1 and S/G2 cell populations or DMSO and Palbociclib
1015 (1μM) treated cells.
1016

Figure S4

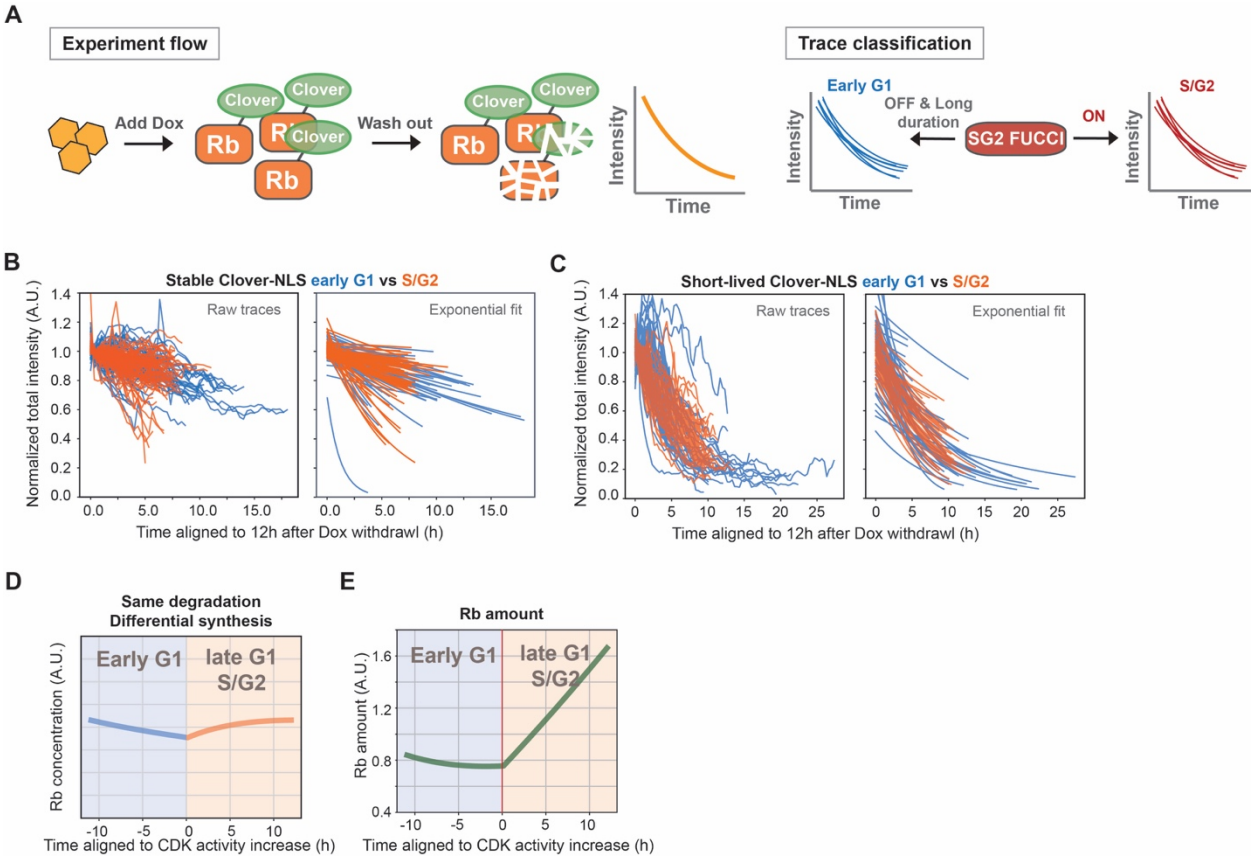

Figure S4. Rb is degraded in early G1 phase.
A. Schematic of the live-cell imaging approach for measuring the protein degradation rate in different cell cycle phases. **B.** Degradation traces for stable Clover-NLS and the corresponding exponential fits (n=88). **C.** Degradation traces of short-lived Clover-NLS and the corresponding exponential fits (n=57). **D-E**. Mathematical model of Rb concentration and protein amount dynamics during cell cycle progression. (D) Rb concentration dynamics assuming that its degradation rate does not change, but its synthesis rate increases by 20% at the G1/S transition as measured in Figure 2A. (E) Total Rb protein amount dynamics assuming that its degradation rate decreases by 80% at the G1/S transition as measured by live imaging (Figure 2C) and its synthesis rate does not change. Related to Figure 2E.

1033 **Figure S5**
1034

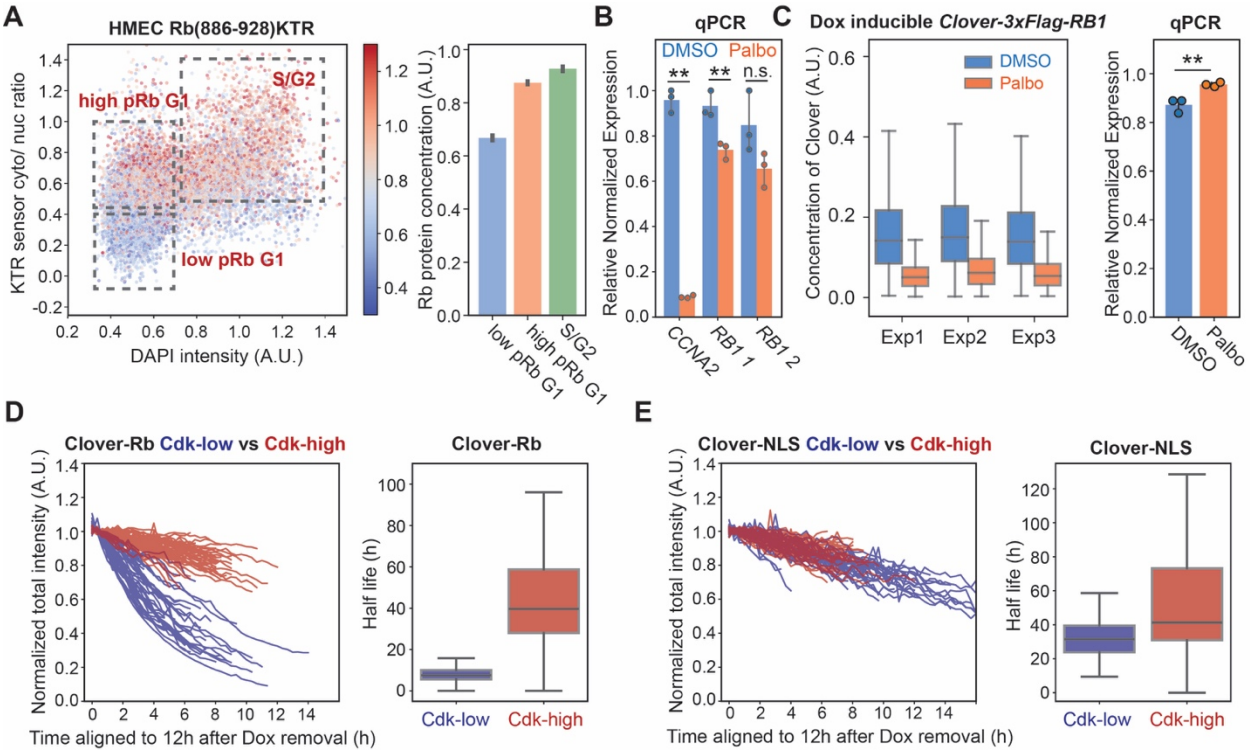

1035
1036

1037 **Figure S5. Rb is stabilized by Cdk mediated phosphorylation**

1038 **A.** Rb concentration in cell populations with different CDK activities. HMEC cells expressing the
1039 Rb(886-928) KTR sensor [36] were stained with an Rb antibody. (Left panel) KTR sensor
1040 cytoplasmic-to-nucleus intensity ratio is plotted against DNA content (DAPI intensity). Dot color
1041 indicates Rb concentration. (Right panel) quantification of Rb concentrations in populations with
1042 different CDK activities as indicated in regions in the left panel. Bars denote 95% confidence
1043 interval for the mean. **B.** *RB1* qPCR measurement of mRNA from cells treated with DMSO or
1044 Palbociclib (1μM, 24 hours); related to Fig. 2B. n=3 and dots denote biological replicates. Bars
1045 denote standard deviation. **C.** Protein and mRNA concentrations of Clover-3xFlag-Rb. Cells
1046 expressing Clover-3xFlag-Rb (Dox induced for 48 hours) were treated with DMSO or
1047 Palbocliclib (1μM) for 24 hours. The protein concentration of Clover-3xFlag-Rb (left panel) was
1048 measured by flow cytometry. The concentration was defined as Clover fluorescent intensity
1049 divided by side scatter area (SSC-A). The mRNA concentration of Clover-3xFlag-Rb (right
1050 panel) was measured using qPCR with primers targeting Clover. **D-E.** (Left panel) The
1051 degradation traces of Clover-3xFlag-Rb protein (D) or Clover-NLS (E) after Dox withdrawal. The
1052 traces were classified into Cdk-low and Cdk-high cells based on the HDHB Cdk sensor. (Right
1053 panel) Distribution of half-lives estimated from the exponential fit. Box plot indicates 5th, 25th,
1054 median, 75th and 95th percentiles.
1055
1056

1057 **Figure S6**

1058

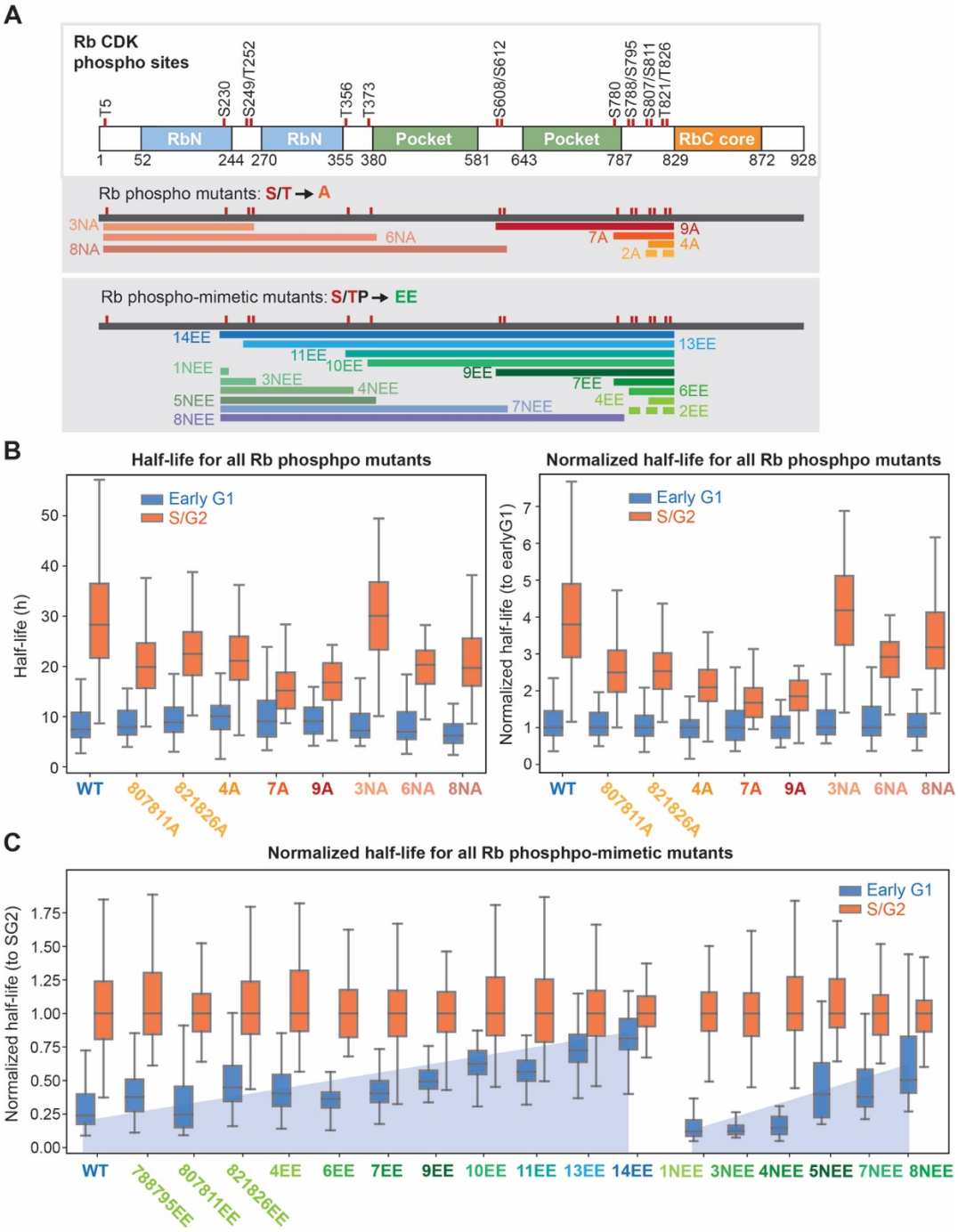

1059

1060

1061 **Figure S6. Half-life measurements of Rb phospho-mutants and phospho-mimetic mutants**
1062 **A.** Schematics of the CDK sites on Rb that were mutated in the Rb phospho-mutants and the
1063 Rb phospho-mimetic mutants used in this study. **B.** The half-lives (left) and normalized half-lives
1064 (right) for all the Rb phospho-mutants measured using the live-cell imaging approach. The
1065 normalized half-lives were calculated by normalizing to the half-life in early G1 for each Rb
1066 protein variant. **C.** Normalized half-lives of all the Rb phospho-mimetic mutants measured using
1067 the live-cell imaging approach. Related to Figure 3E, F. Here, the normalized half-lives were
1068 calculated by normalizing to the half-life in S/G2 for each Rb protein variant.
1069

1070 **Figure S7**
1071

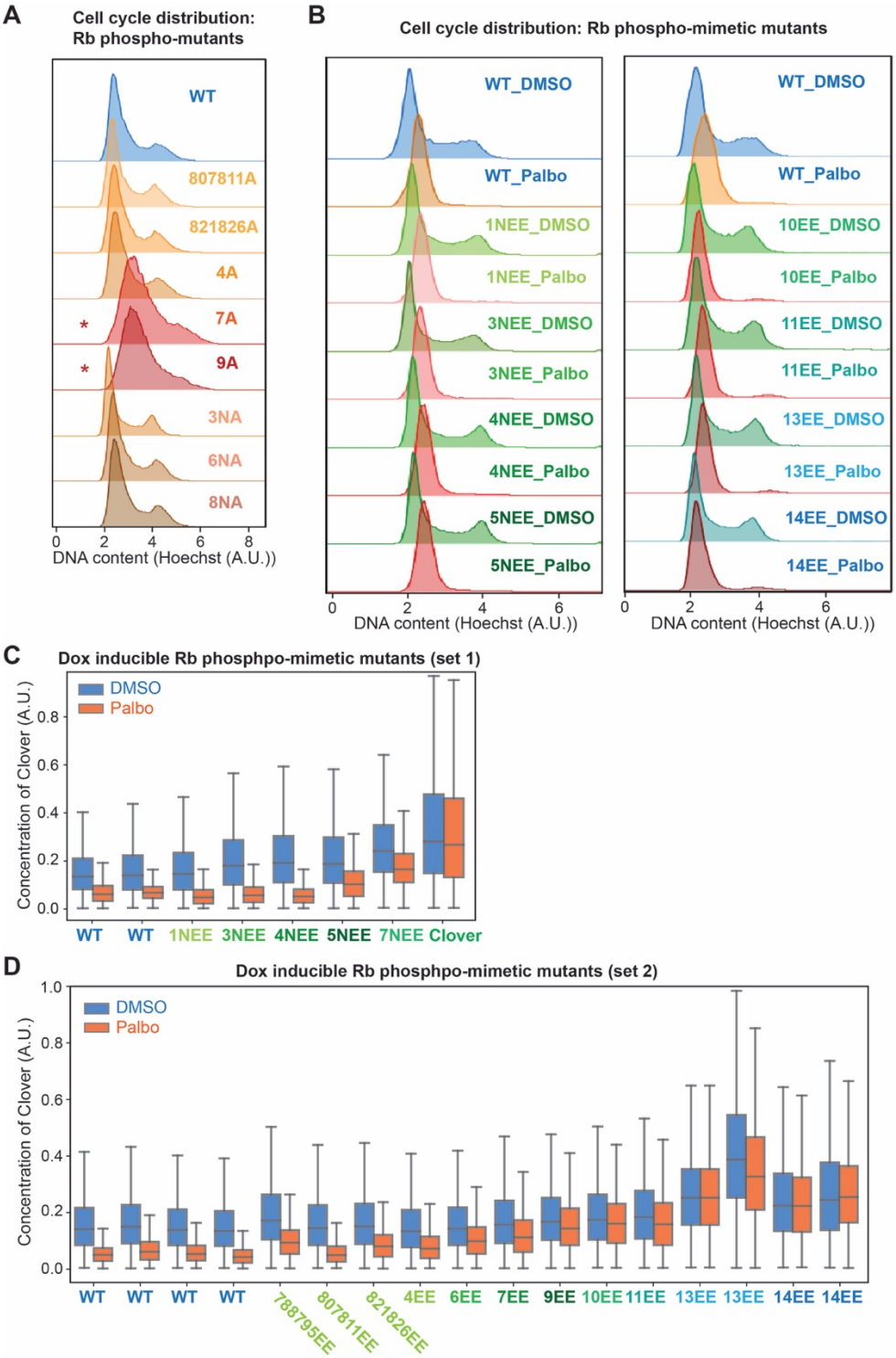

1072
1073

1074 **Figure S7. Cdk phospho-site mutations affect Rb stability**
1075 **A.** Cell cycle distribution for cells expressing different Rb phospho-mutants. Cells expressing
1076 Clover-3xFlag-Rb phospho-mutants (Dox induced for 48 hours) were incubated with Hoechst for
1077 30 minutes to stain DNA, and then analyzed by flow cytometry. Red stars indicate that cells
1078 expressing Rb7A and Rb9A are arrested in G1. **B.** Cell cycle distribution for cells expressing Rb
1079 phospho-mimetic mutants. Cells expressing Clover-3xFlag-Rb phospho-mimetic mutants (Dox
1080 induced for 48 hours) were treated with DMSO or Palbocliclib (1μM) for 24 hours. Then the cells
1081 were incubated with Hoechst for 30 minutes to stain DNA, and analyzed by flow cytometry. **C-D**.
1082 The concentrations of Clover-3xFlag-Rb phospho-mimetic mutants (induced by Dox for 48
1083 hours) after 24 hours of DMSO or Palbociclib (1μM) treatment, as measured by flow cytometry.
1084 (**C**) shows the mutations made from the N-terminus of Rb, and (**D**) shows the mutations made
1085 from the C-terminus of Rb.
1086
1087

1088 **Figure S8**
1089

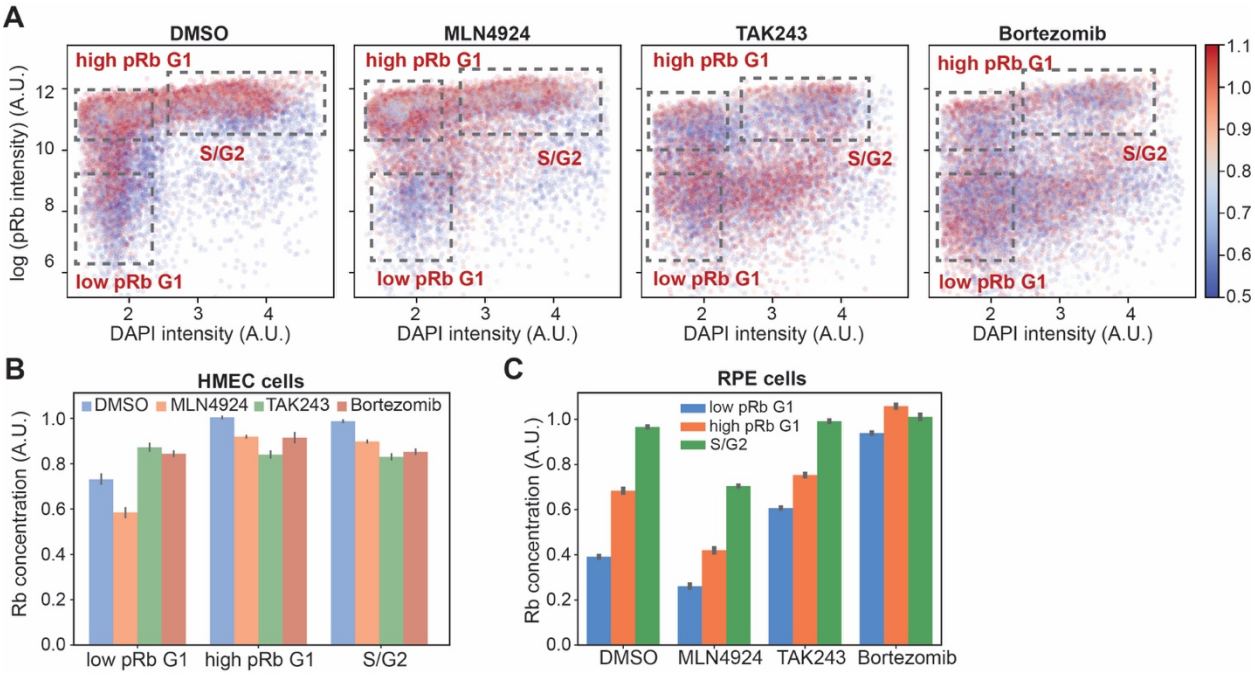

1090
1091
1092 **Figure S8. Un/hypo-phosphorylated Rb is degraded through the Ubiquitin-proteasome**
1093 **system**
1094 **A.** HMEC cells were treated with the indicated drugs for 5 hours, fixed, and stained with
1095 phospho-Rb (S807/811) and Rb antibodies. The Rb concentration is calculated by dividing total
1096 Rb intensity by nuclear area$^{3/2}$. The dot color indicates Rb concentration. **B**. Rb concentration in
1097 different phospho-Rb populations of HMEC cells shown in A. **C.** Rb concentration in different
1098 phospho-Rb populations of RPE-1 cells after treatments with the indicated drugs for 6 hours, as
1099 measured by flow cytometry. Rb concentration was calculated by dividing the Rb total intensity
1100 with the side scatter area (SSC-A).
1101
1102

1103 **Figure S9**
1104

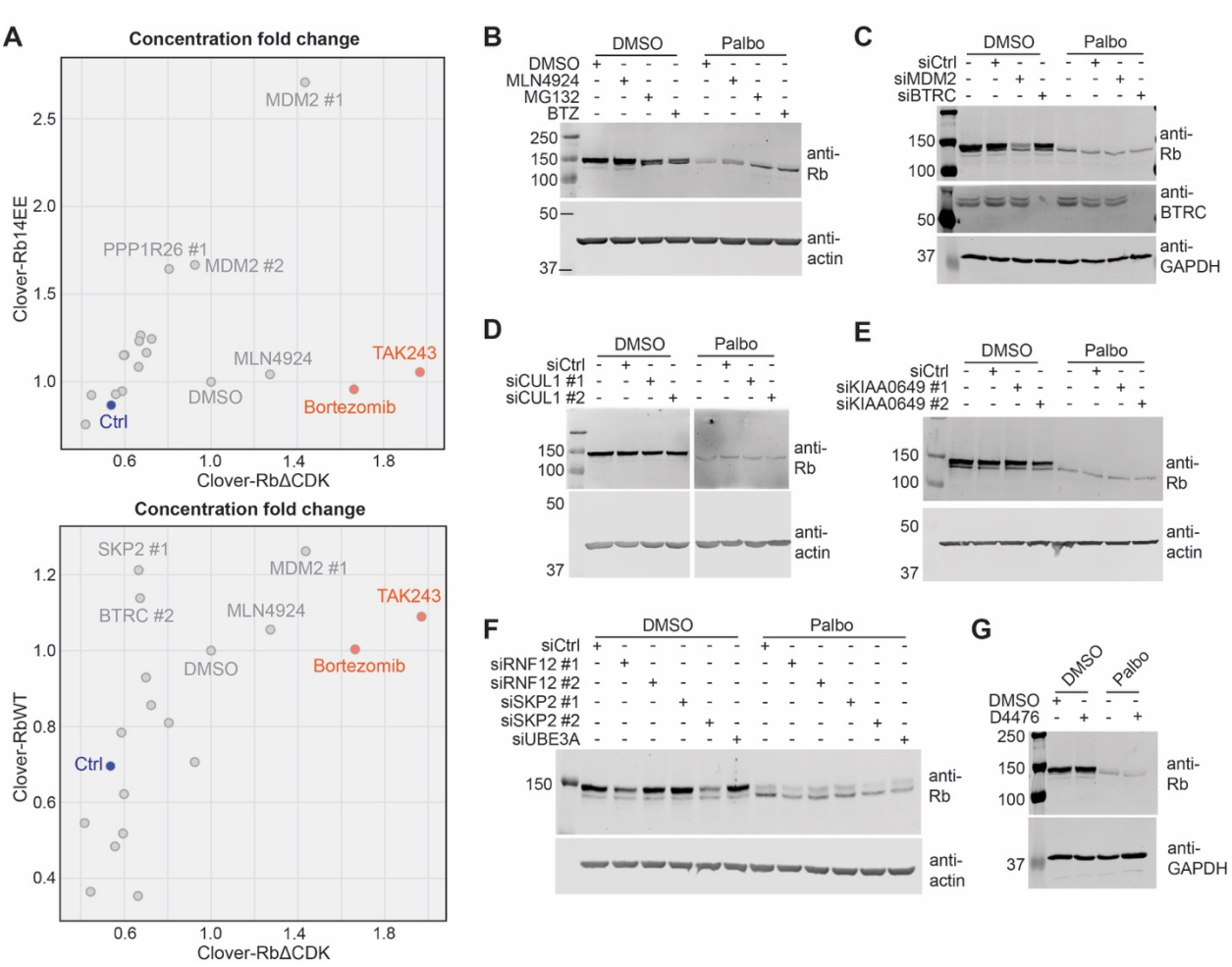

1105
1106
1107 **Figure S9. Examination of E3 ligases reported to target Rb**
1108 **A.** Comparison of concentration fold change after siRNA treatment. HMEC cells expressing
1109 Clover-3xFlag-RbΔCDK, Clover-3xFlag-RbWT, or Clover-3xFlag-Rb14EE (Dox induced for 48
1110 hours) were transfected with siRNAs against the published E3 ligase genes for 48 hours. Then,
1111 the cells were fixed and imaged. The concentration fold change is calculated by dividing the
1112 Clover concentration of the treatment well by the concentration in the DMSO treated well. Red
1113 dots indicate the positive controls, *i.e.*, TAK243 and Bortezomib treatments (5 hours of
1114 treatment), and the blue dot indicates the siCtrl treated sample. **B-F**. The published E3 ligase
1115 genes for Rb were also examined by western blot analysis. HMEC cells were transfected with
1116 the corresponding siRNAs for 24 hours, and then treated with DMSO or Palbociclib (1μM) for 24
1117 hours. Cells were then harvested for western blotting with Rb antibodies. The lower band in the
1118 Rb western blots represents un/hypo-phosphorylated Rb. **G.** The effect of CK1 on Rb half-life
1119 was examined using western blot analysis. Cells were treated with DMSO vs Palbociclib (1μM)
1120 and DMSO vs D4476 (25μM CK1 inhibitor), and then the cells were lysed for western blotting.
1121

1122 **Figure S10**

1123

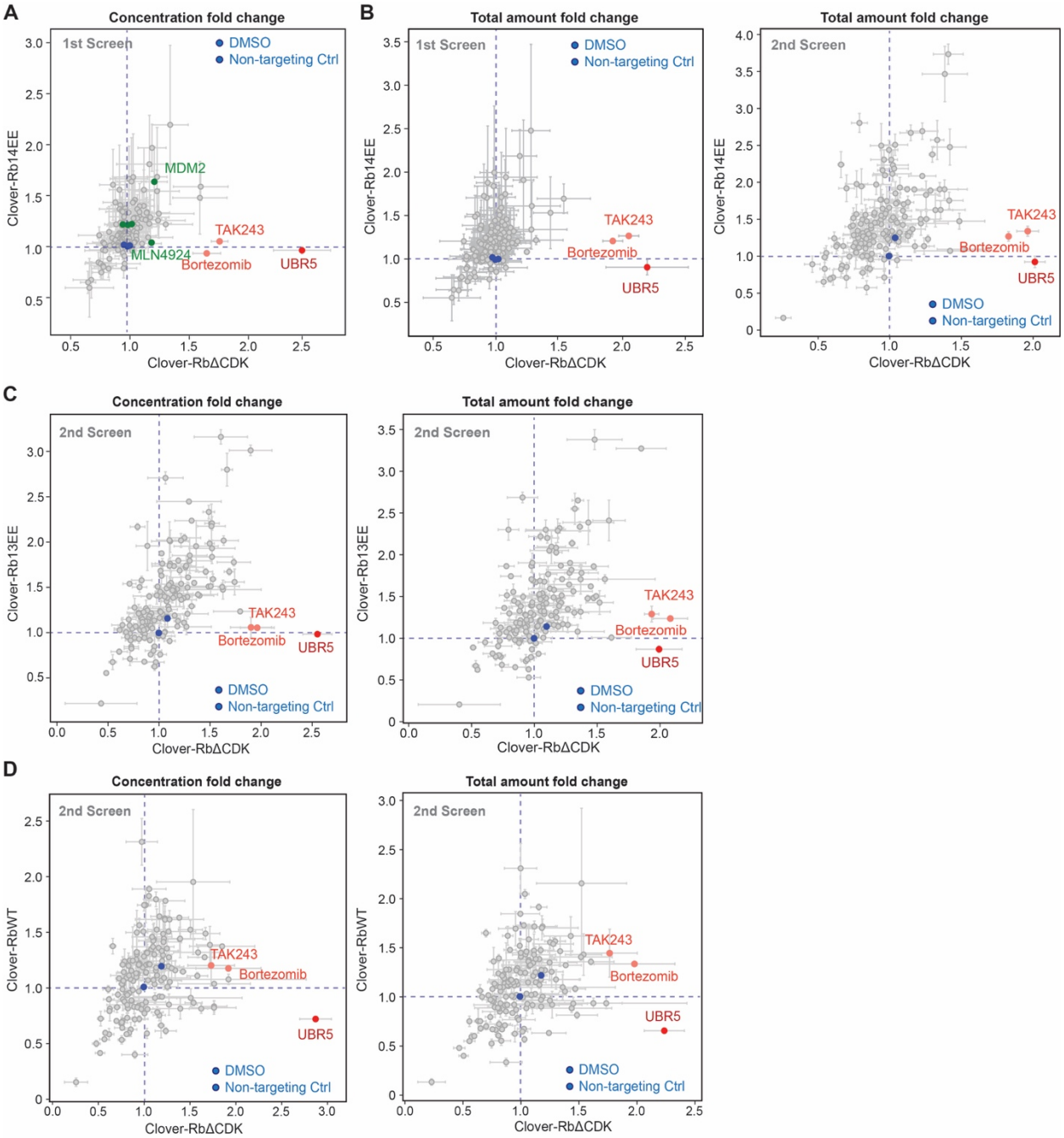

1124

1125

1126

1127
1128 **Figure S10. UBR5 is identified as a candidate E3 ligase targeting Rb in siRNA screens**
1129 **A.** Same plot as Figure 4D (1st siRNA screen), except that the green dots are added to indicate
1130 the previously reported E3 genes for Rb. **B.** The total amount fold changes of Clover-3xFlag-
1131 RbΔCDK and Clover-3xFlag-Rb14EE are plotted. Related to Figure 4D, E. **C.** Concentration fold
1132 changes and total amount fold changes of Clover-3xFlag-RbΔCDK and Clover-3xFlag-Rb13EE
1133 from the 2nd siRNA screen. n = 2 biological replicates. **D.** Concentration fold changes and total
1134 amount fold changes of Clover-3xFlag-RbΔCDK and Clover-3xFlag-RbWT from the 2nd siRNA
1135 screen. n = 2 biological replicates.
1136

Figure S11

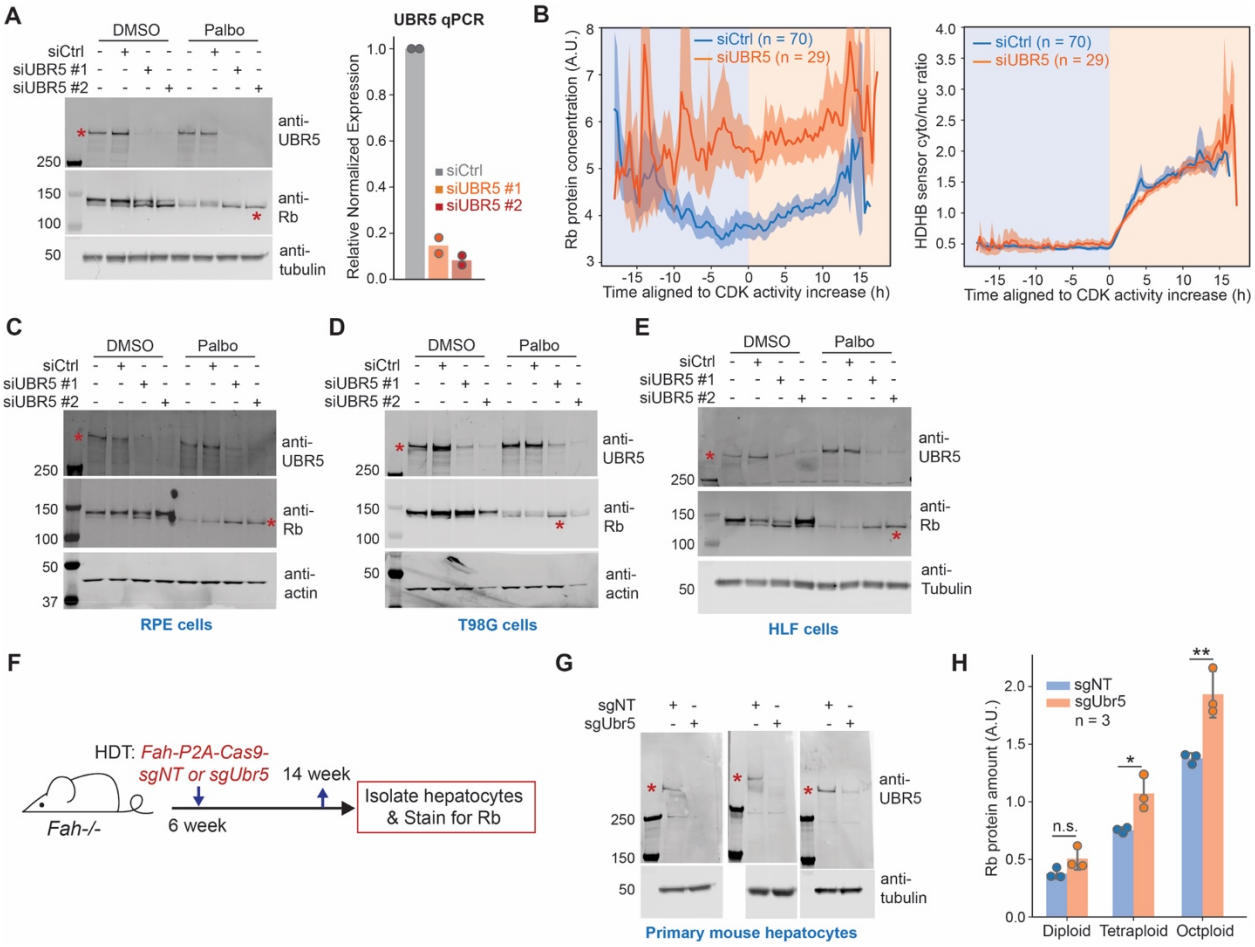
A
DMSO
Palbo
siCtrl
siUBR5 #1
siUBR5 #2
anti-UBR5
anti-Rb
anti-tubulin
UBR5 qPCR
Relative Normalized Expression
siCtrl
siUBR5 #1
siUBR5 #2
B
siCtrl (n = 70)
siUBR5 (n = 29)
Rb protein concentration (A.U.)
HDHB sensor cyto/nuc ratio
Time aligned to CDK activity increase (h)
C
RPE cells
D
T98G cells
anti-actin
E
HLF cells
anti-Tubulin

F
HDT: Fah-P2A-Cas9-sgNT or sgUbr5
14 week
Fah-/-
6 week
Isolate hepatocytes & Stain for Rb
G
sgNT
sgUbr5
anti-UBR5
anti-tubulin
Primary mouse hepatocytes
H
sgNT
sgUbr5
n = 3
Rb protein amount (A.U.)
n.s.
Diploid
Tetraploid
Octploid

1141 **Figure S11. UBR5 is responsible for Rb degradation in multiple cell types**
1142 **A.** Left panel: Immunoblot of Rb after UBR5 knockdown by siRNA. Cells were treated with
1143 siRNAs for 24 hours, and then treated with DMSO or Palbociclib (1μM) for 24 hours before
1144 harvest. The lower band in the Rb blot indicates the un/hypo-phosphorylated Rb (marked by red
1145 star). Right panel: qPCR validation of UBR5 knockdown efficiency. HMEC cells were
1146 transfected with siRNA for 48 hours. **B.** Live imaging validation of Rb concentration dynamics
1147 during cell cycle progression. HMEC cells expressing an endogenously tagged *RB1-3xFLAG-*
1148 *Clover-sfGFP* and an HDHB CDK sensor [1] were transfected with UBR5 siRNA for 24 hours and
1149 then imaged. Average traces for Rb-3xFLAG-Clover-sfGFP concentration (left panel) or the
1150 cytoplasmic-to-nuclear intensity ratio of the HDHB sensor (right panel) are plotted; solid lines
1151 indicate mean values for each time point and shaded regions indicate the standard deviation of
1152 the mean. Traces are aligned using the HDHB sensor to identify the time that CDK activity
1153 begins to increase. **C-E.** Western blot validation of the role of UBR5 in Rb degradation in
1154 multiple cell lines (**C.** RPE cells, **D.** T98G cells, **E.** HLF cells). Cells were transfected with
1155 siRNAs against UBR5 or Ctrl siRNA. 24 hours later, DMSO or Palbociclib (1μM) were added for
1156 another 24 hours. Then, cells were lysed for western blot analysis. The lower band of the Rb
1157 blot is marked by a red star, which represents the un/hypo-phosphorylated Rb. **F**. Experimental
1158 flow of the *Fah-/-* mouse liver model. 6-week old *Fah-/-* mice were hydrodynamically transfected
1159 with plasmids carrying an *Fah-P2A-Cas9-sgNT* transposon or an *Fah-P2A-Cas9-sgUbr5*
1160 transposon, together with a transposase plasmid. 8 weeks later, hepatocytes were isolated from
1161 the mice for downstream analysis. **G.** Western blot validation of UBR5 knockout efficiency in
1162 primary hepatocytes. *Fah-/-* mice were injected with transposons carrying *Cas9-sgNT* or *Cas9-*
1163 *sgUbr5*. Primary hepatocytes were isolated from the mice, plated, and then lysed for western
1164 blot analysis. n = 3 pairs of mice. **H.** Total Rb amount in the low-phospho-Rb population of the
1165 primary hepatocytes isolated from mice receiving *Fah-P2A-Cas9-sgNT* or *Fah-P2A-Cas9-*
1166 *sgUbr5* transposons. n = 3 pairs of mice. Error bar indicates standard deviation. Related to
1167 Figure 5D.
1168

1169 **Figure S12**
1170

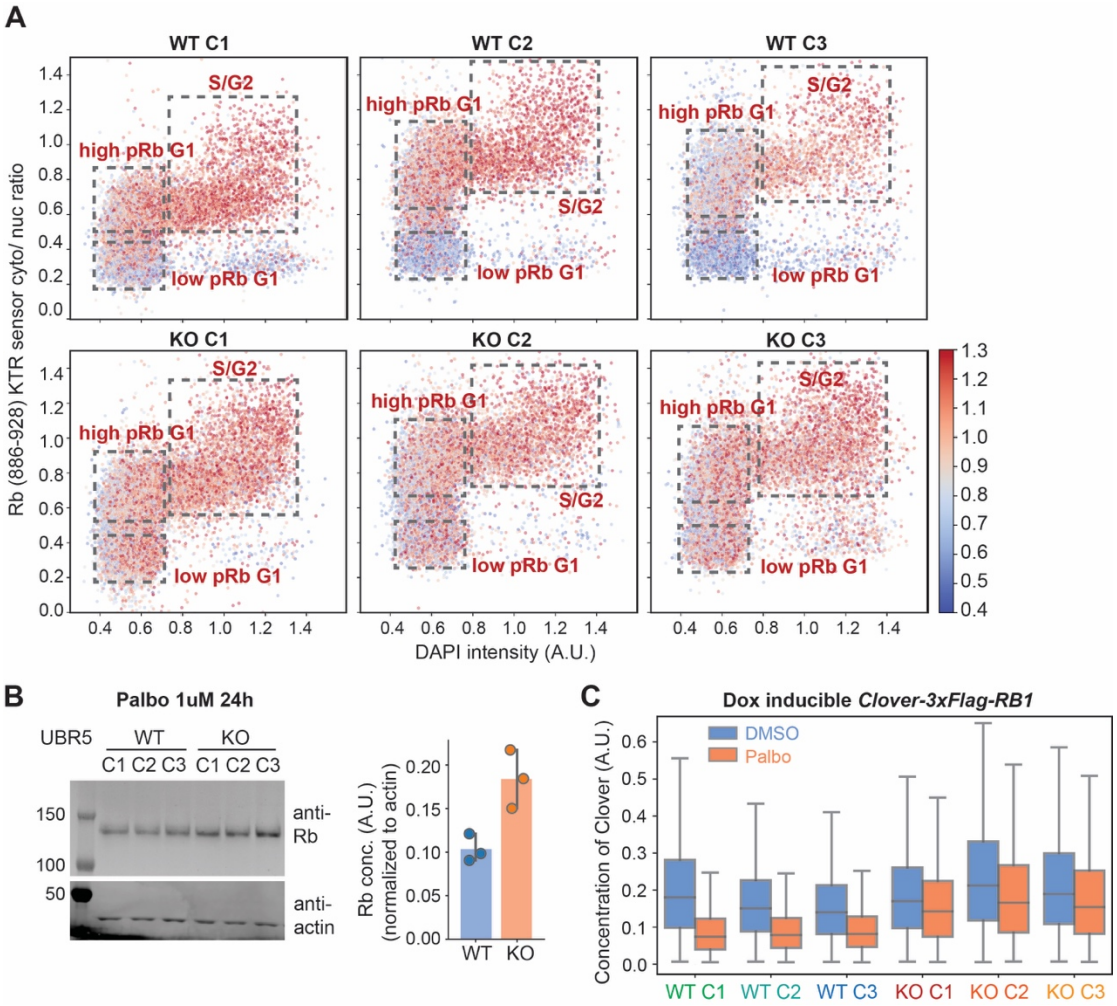

1171
1172
1173 **Figure S12. Rb concentration is increased in the low-phospho-Rb populations of *UBR5***
1174 ***KO* clonal cell lines**
1175 **A**. Rb staining of *UBR5 WT* or *KO* clonal cell lines expressing the Rb (886-928) KTR sensor [36].
1176 The cytoplasmic-to-nucleus intensity ratio of the KTR sensor is plotted against DNA content
1177 (DAPI). The dot color indicates the Rb concentration. Related to Fig. 4B. **B.** Western blot
1178 analysis of Rb concentration after Palbociclib treatment in UBR5 clonal cell lines. 6 UBR5 clonal
1179 cell lines (3 WT, 3 KO) were treated with DMSO or Palbociclib (1μM) for 24 hours, and then
1180 lysed for western blotting. Quantification of Rb concentration (Rb band intensity normalized to
1181 the actin band intensity) is shown on the right. Dots denote individual clones and error bars
1182 denote the standard deviation. **C.** Flow cytometry analysis of Clover-3xFlag-Rb concentration
1183 after Palbociclib treatment. 6 UBR5 clonal cell lines (3 WT, 3 KO) expressing Clover-3xFlag-
1184 RbWT (Dox induced for 48 hours) were treated with DMSO or Palbociclib (1μM) for 24 hours,
1185 and then cells were analyzed using flow cytometry. The concentration of Clover-3xFlag-RbWT
1186 was defined as Clover fluorescent intensity divided by side scatter area (SSC-A).
1187

1188 **Figure S13**

1189

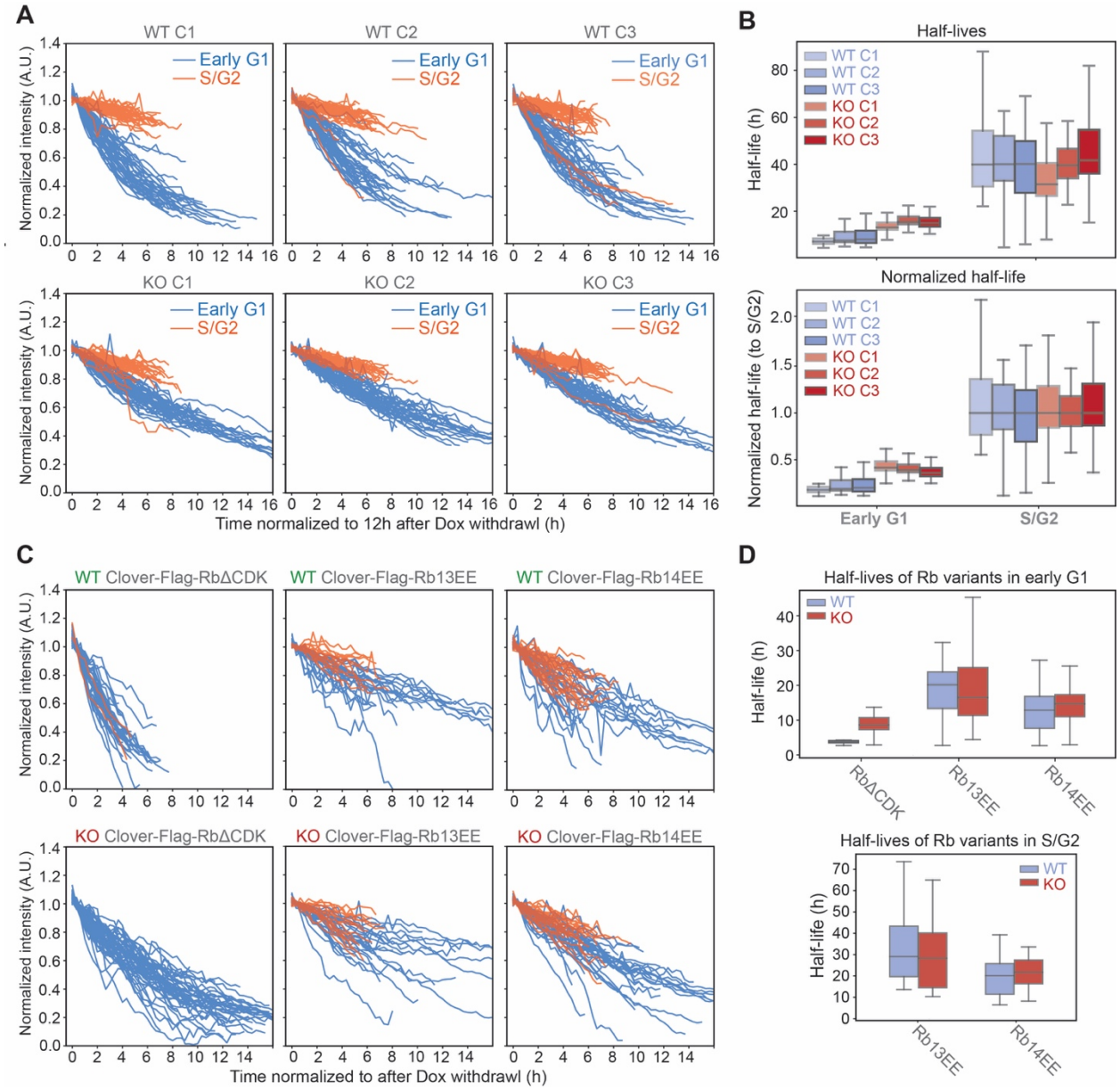

1190

1191

1192

1193 **Figure S13. Un-phosphorylated Rb is stabilized in *UBR5 KO* cells**
1194 **A.** The degradation traces of Clover-3xFlag-RbWT protein after Dox withdrawal in 6 UBR5
1195 clonal cell lines (3 WT, 3 KO). The traces were classified into early G1 phase or S/G2 phase
1196 based on the FUCCI cell cycle reporter. **B.** The half-life distributions (upper panel) and
1197 normalized half-lives (lower panel, normalized to the median of S/G2 half-life) calculated from
1198 the degradation traces shown in (**A**). **C**. The degradation traces of Clover-3xFlag-RbΔCDK,
1199 Clover-3xFlag-Rb13EE, and Clover-3xFlag-Rb14EE protein after Dox withdrawal in UBR5 WT
1200 and KO cell lines. The traces were classified into early G1 phase or S/G2 phase based on a
1201 FUCCI cell cycle reporter. **D**. The half-life distributions of the Rb variants in (C) in early G1
1202 phase (upper panel) or in S/G phase (lower panel) calculated from the degradation traces
1203 shown in (C).
1204

1205 **Figure S14**
1206

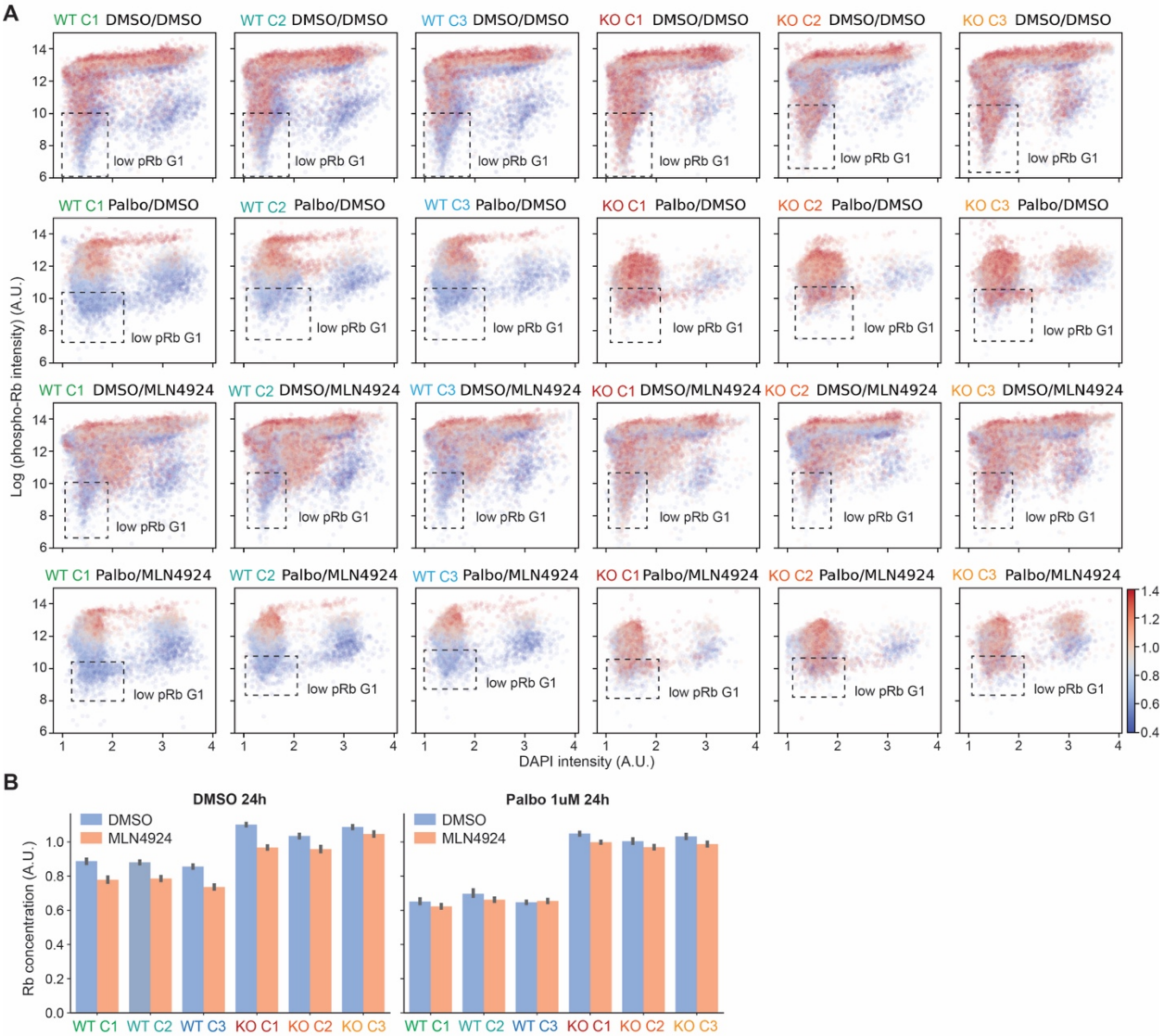

1207
1208
1209 **Figure S14. The Rb concentration is increased in the low-phospho-Rb populations of**
1210 ***UBR5 KO* clonal cell lines**
1211 **A.** phospho-Rb concentration is plotted against DNA content in UBR5 clonal cell lines. 6 UBR5
1212 clonal cell lines (3 WT, 3 KO) were treated with DMSO or Palbociclib (1μM) for 24 hours, and
1213 then the cells were treated with DMSO or MLN4924 (1μM) for 5 hours before fixation. Cells
1214 were stained with phospho-Rb (S807/811) and Rb antibodies, followed by imaging. The dot
1215 color indicates the Rb concentration. The dashed line box indicates the low pRb G1 population
1216 that has low concentration of phospho-Rb. Plot titles indicate the cell genotype and the
1217 treatments administered. *E.g.*, Palbo/DMSO indicates that 1 μM Palbociclib was administered
1218 before DMSO. **B.** Quantification of the Rb concentration in the low pRb G1 populations of cells
1219 in (A). Error bar indicates the 95% confidence interval of the mean.
1220
1221
1222

1223 **Figure S15**

1224

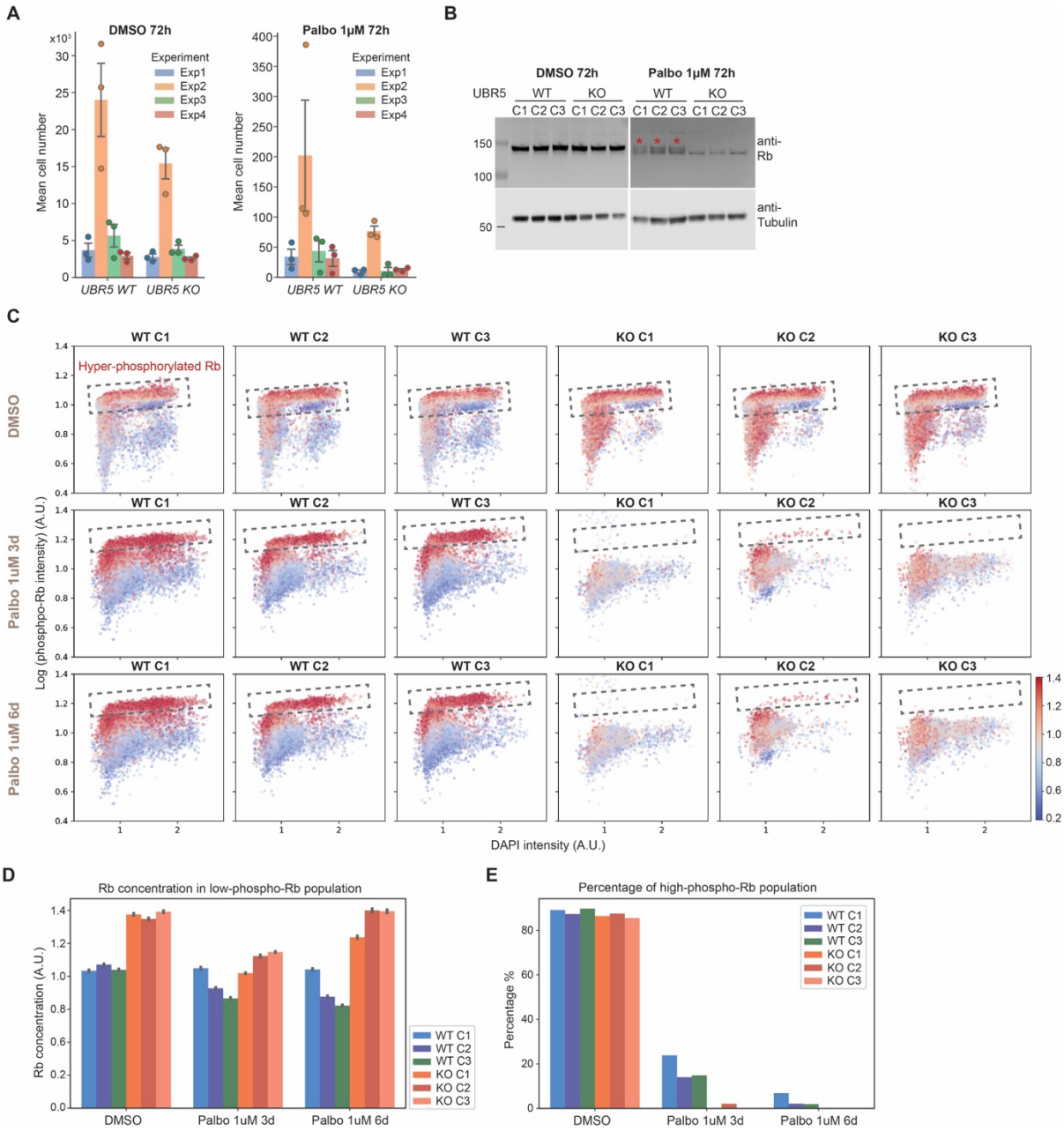

1225

1226

1227 **Figure S15. *UBR5 KO* cells are sensitized to Palbociclib treatment**
1228 **A.** The absolute cell number counts for 6 UBR5 clonal cell lines (3 WT, 3 KO) after DMSO or
1229 Palbociclib (1μM) treatment for 72 hours; related to Fig. 4E. **B-C.** Western blot (**B**) and
1230 immunostaining (**C**) analysis of phospho-Rb (S807/811) in 6 UBR5 clonal cell lines (3 WT, 3
1231 KO) after DMSO or Palbociclib (1μM) treatment for 3 days or 6 days. The hyper-phosphorylated
1232 Rb population is marked using red stars (the upper band in (B)) or dashed lined boxes (in (C)).
1233 **D**. Quantification of the Rb concentration in the low pRb G1 populations of cells in (C). Error bar
1234 indicates the 95% confidence interval of the mean. **E**. Quantification of the percentage of hyper-
1235 phosphorylated Rb population of cells in (C).
1236
1237
1238

1239 **Figure S16**
1240

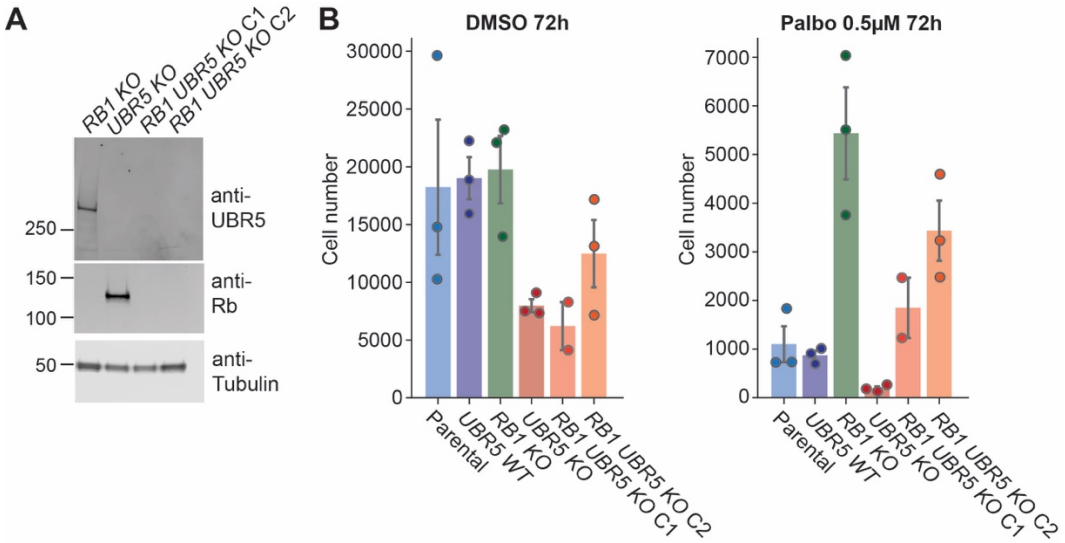

1241
1242
1243 **Figure S16. The increased sensitivity to Palbocilib treatment in *UBR5 KO* cells depends**
1244 **on Rb.**
1245 **A.** Western blot validation of UBR5 and Rb double KO cell lines. **B**. The absolute cell number
1246 count for wild-type, *UBR5 KO*, *RB1 KO*, and *UBR5 RB1 KO* cells after DMSO or Palbociclib
1247 (0.5μM) treatment for 72 hours; related to Fig. 4F. Bars denote the standard deviation of the
1248 mean.
1249

1250 **Figure S17**
1251

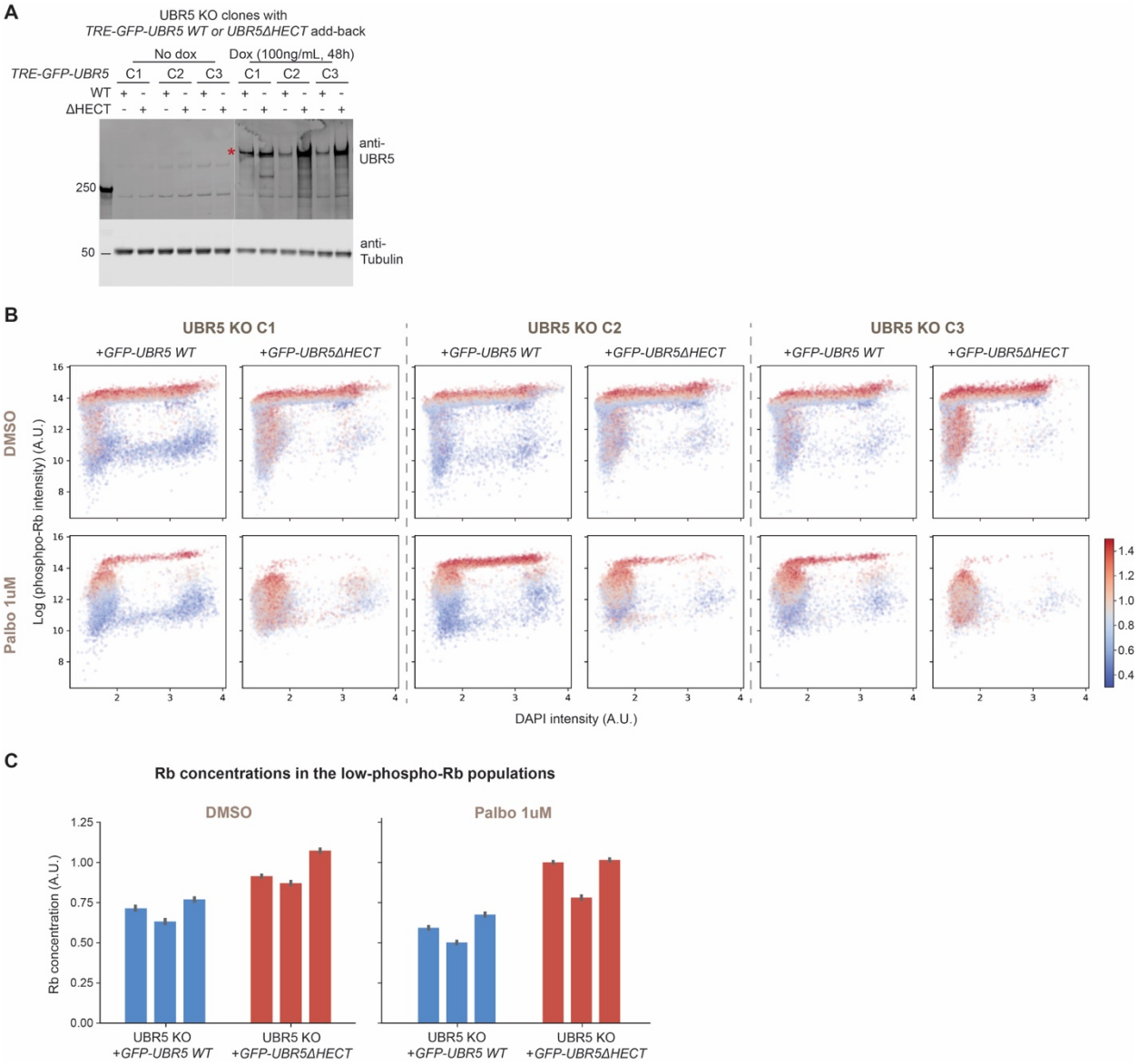

1252
1253
1254 **Figure S17. Adding back WT UBR5, but not mutant UBR5, decreases Rb concentration in**
1255 ***UBR5 KO* cells**
1256 **A.** Western blot validation of *UBR5 KO* cell lines (3 KO clones) with UBR5WT or UBR5ΔHECT
1257 add-back using the Dox inducible system. Cells were induced with Dox (100ng/ml) for 48 hours
1258 and then lysed for western blot analysis. **B**. immunostaining analysis of phospho-Rb (S807/811)
1259 in 3 *UBR5 KO* clonal cell lines with UBR5WT or UBR5ΔHECT add-back (as described in A)
1260 after DMSO or Palbociclib (1μM) treatment for 24 hours. The dot color indicates the Rb
1261 concentration. **C**. Quantification of the Rb concentration in the low-pRb G1 populations of cells
1262 in (B). Error bar indicates the 95% confidence interval of the mean.
1263

1264 **Figure S18**
1265

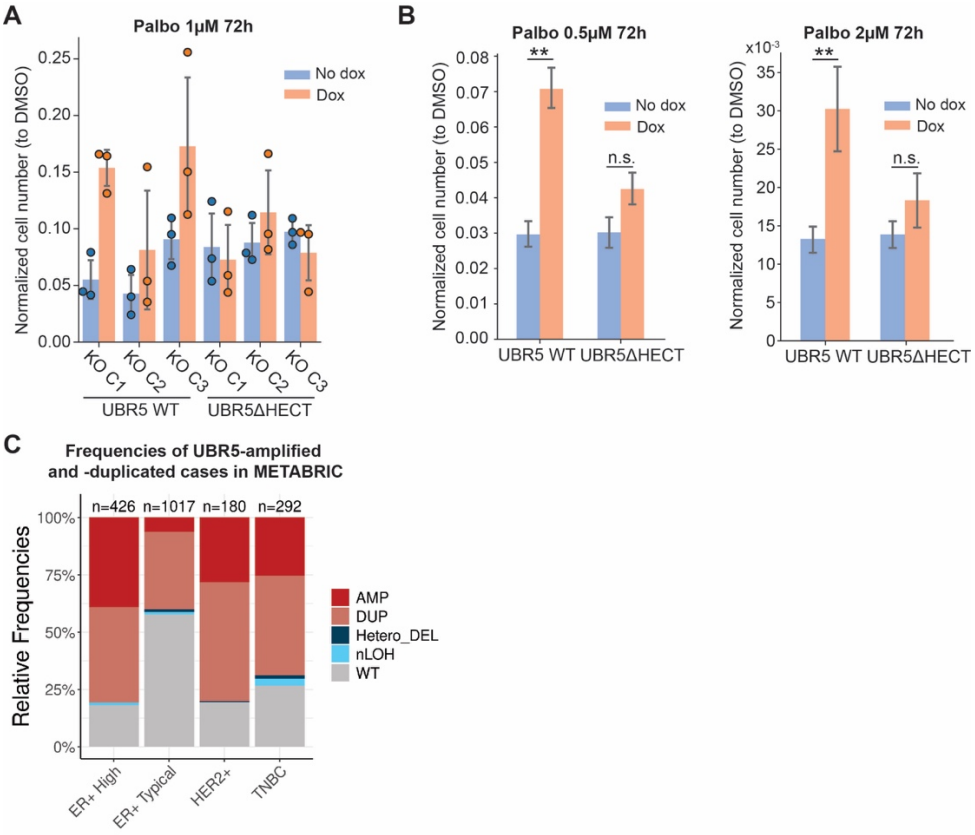

1266
1267
1268 **Figure S18. Adding back WT URB5 rescues the Palbociclib-sensitivity phenotype.**
1269 **A.** Normalized cell number of *UBR5 KO* cells with UBR5 WT or UBR5ΔHECT addback after
1270 Palbociclib (0.5μM) treatment for 72 hours (related to Fig. 4G). **B.** Normalized cell number of
1271 *UBR5 KO* cells with UBR5 WT or UBR5ΔHECT addback after Palbociclib (0.5μM or 2μM)
1272 treatment for 72 hours. The results are the average of 3 *UBR5 KO* clonal cell lines with different
1273 UBR5 addback and 3 biological replicates. All error bars denote standard deviations. **C.**
1274 Frequencies of *UBR5*-amplification and -duplication in the METABRIC dataset across different
1275 breast cancer subtypes. The number of tumors within each group is indicated on the top of each
1276 bar. AMP = amplification with total copy number ≥ 6; DUP = duplication with total copy number ≥
1277 3; Hetero_DEL = heterozygous deletion; nLOH = neutral loss-of-heterozygosity.
1278
1279

Materials and Methods

Mice

All mice were handled in accordance with the guidelines of the Institutional Animal Care and Use Committee at Stanford University. The *Fah*$^{-/-}$ mice were kindly shared by Dr. Markus Grompe's group at Oregon Health & Science University. At 6 weeks old, the *Fah*$^{-/-}$ mice were subjected to hydrodynamical transfection through their tail vein. We injected one plasmid containing a transposon that carries *Fah*, *Cas9*, and a guide RNA, and a second plasmid containing the transposase SB100. The plasmid backbone was kindly provided by Dr. Hao Zhu's lab at UT Southwestern Medical Center. We modified the guide RNA sequence on the transposons to either a negative control guide RNA sequence or a guide RNA targeting the *Ubr5* gene. 8 weeks after the injection, the mice were sacrificed to isolate primary hepatocytes.

Cell culture conditions and cell lines

All cells were cultured at 37ºC with 5% CO_2. Non-transformed hTERT1-immortalized human mammary epithelium cells (HMEC) were obtained from Stephen Elledge's laboratory at Harvard Medical School[73] and cultured in MEGM™ Mammary Epithelial Cell Growth Medium (Lonza CC-3150). In microscopy experiments we used the same media but without phenol red to reduce background fluorescence (Lonza CC-3153 phenol-red free basal media supplemented with growth factors and other components from the Lonza CC4136 kit). T98G cells were purchased from ATCC, recently isolated primary fetal human lung fibroblasts (HLF) were purchased from Cell Applications, and hTERT1-immortalized retinal pigment epithelium (RPE-1) cells were obtained from the Cyert laboratory at Stanford. All these cell lines were grown in Dulbecco's modification of Eagle's medium (DMEM) with L-glutamine, 4.5 g/l glucose, and sodium pyruvate (Corning), supplemented with 10% FBS (Corning) and 1% penicillin/streptomycin.

Fluorescent reporter cell lines

The S/G2 component of the FUCCI cell cycle reporter – mCherry-Geminin – was cloned into the CSII-EF-MCS lentiviral vector backbone under a constitutive EF1α promoter[1]. The CSII vector, the lentiviral packaging vector dr8.74, and the envelope vector VSVg were transfected into HEK 293T cells by PEI (1mg/mL, Sigma-Aldrich). 48 hours later, the lentivirus-containing medium was collected and used to infect HMEC cells. 2-3 days after infection, positive cells were sorted by FACS and expanded. The endogenously tagged *RB1-3xFLAG-Clover-sfGFP* HMEC cell line was created by Evgeny Zatulovskiy[26].

Inducible expression of wild-type and mutant Rb in cell lines

To inducibly express wild-type Rb and Rb mutants in cells, we used the doxycycline-inducible Rb cassette published in[29], and performed site-directed mutagenesis (E0554S, NEB) to generate Rb mutant plasmids. All the plasmids contained the wild-type *RB1* gene or *RB1* mutants fused with fluorescent Clover and 3xFLAG affinity tag sequences, a zeocin resistance gene, and a Tet-On 3G transactivator gene driven by the EF1α promoter. The HMEC cell lines stably expressing doxycycline-inducible Rb variants were generated by transfecting cells with 1 µg of doxycycline-inducible plasmid and 1 µg of PiggyBac Transposase plasmid using the FuGene HD reagent (Promega E2311). Zeocin (300 µg/ml) selection began two days after transfection and lasted for at least 2 weeks until all the cells became resistant.

UBR5 knockout cell lines and *RB1* knockout cell lines

UBR5 knockout HMEC cells and *RB1* knockout HMEC cells were generated using the CRISPR knockout kit v2 from Synthego following the manufacturer's protocol. Briefly, the Ribonucleoprotein (RNP) complexes (9:1 sgRNA to Cas9 ratio) were assembled in Nucleofector Solution plus Supplement (Lonza Amaxa HMEC Nucleofector Kit) to a total volume of 100µL. The

1331 RNP was incubated at room temperature for 10 minutes. 0.5 million HMEC cells were
1332 resuspended in 100μL RNP solution and transferred to a cuvette. This was followed by
1333 electroporation using the Lonza nucleofector 2b device (program Y-001). 48 hours later, the
1334 knockout efficiency was examined by western blot. In both cases, we obtained about 40-50%
1335 knockout efficiency. The resulting cell populations were then single cell sorted to make clonal cell
1336 lines. After single cell expansion, the grown out clones were validated for *RB1* or *UBR5* knockout,
1337 and wild-type clones and knockout clones were kept for further analysis. The *UBR5 RB1* double
1338 knockout cell lines were generated by knocking out the *RB1* gene in the *UBR5* knockout clones.
1339

1340 **Primary hepatocyte isolation and 2D culture**

1341 Primary hepatocytes were isolated by two-step collagenase perfusion[74] using liver perfusion
1342 medium (Thermo Fisher Scientific, 17701038), liver digest medium (Thermo Fisher Scientific,
1343 17703034), and hepatocyte wash medium (Thermo Fisher Scientific, 17704024). The protocol for
1344 2D culture of primary hepatocytes was kindly shared by Yinhua Jin from Dr. Roeland Nusse's lab
1345 at Stanford University[75]. Briefly, primary hepatocytes from *Fah-/-* mice were isolated by two-step
1346 collagenase perfusion. After isolation, cells were washed 3 times with hepatocyte wash medium
1347 (Thermo Fisher Scientific, 17704024). Cells were then plated in a 6-well plate precoated with
1348 collagen I (50μg/mL) at a density of 200,000 cells per well. The culture medium contained 3μM
1349 CHIR99021 (Peprotech), 25ng/mL EGF (Peprotech), 50ng/mL HGF (Peprotech), and 100ng/mL
1350 TNFa (Peprotech) in Basal medium. The Basal medium contained William's E medium (GIBCO),
1351 1% Glutamax (GIBCO), 1% Non-Essential Amino Acids (GIBCO), 1% Penicillin/streptomycin
1352 (GIBCO), 0.2% normocin (Invitrogen), 2% B27 (GIBCO), 1% N2 supplement (GIBCO), 2% FBS
1353 (Corning), 10mM nicotinamide (Sigma), 1.25mM N-acetylcysteine (Sigma), 10μM Y27632
1354 (Peprotech), and 1μM A83-01 (Tocris). The culture medium was refreshed every other day. Cells
1355 were passaged via trypsinization using TrypLE (Thermo-Fisher). The first passage cells were
1356 used for immunostaining or western blot analysis.
1357

1358 **Live cell imaging and analysis**

1359 The cells for imaging were seeded on 35-mm glass-bottom dishes (MatTek) one day before
1360 imaging. Then, the cells were transferred to a Zeiss Axio Observer Z1 microscope equipped with
1361 an incubation chamber and imaged for 48 hours at 37°C and 5% CO_2. Brightfield and fluorescence
1362 images were collected at multiple positions every 20 minutes using an automated stage controlled
1363 by the Micro-Manager software. We used a Zyla 5.5 sCMOS camera and an A-plan 10x/0.25NA
1364 Ph1 objective. For half-life measurements, cells were plated in doxycycline containing medium
1365 (1μg/mL) and induced for 36 hours. After this induction, the doxycycline-containing medium was
1366 removed, the cells were washed once with fresh doxycycline-free medium, and then, once the
1367 fresh medium lacking doxycycline was added, the cells were transferred to the microscope for
1368 imaging. For most of the Rb mutants, the half-life analysis started 12 hours after doxycycline
1369 removal to eliminate the potential effect of protein synthesis from residual mRNA. For the fast
1370 degraded Rb mutants, e.g., RbΔCDK, the half-life analysis started 3 hours after doxycycline
1371 removal to ensure the signal-to-noise ratio is good enough for accurate quantification. The cell
1372 cycle stage was classified using an mCherry-Geminin FUCCI sensor. The early G1 phase traces
1373 were taken as those having no mCherry-Geminin expression that lasted longer than 7 hours. The
1374 S/G2 phase is defined by mCherry-Geminin FUCCI marker expression. For cells expressing the
1375 HDHB CDK sensor[25], the transition from low CDK activity to high CDK activity was taken as the
1376 inflection point of the cytoplasm-to-nuclear fluorescence ratio [25]. The volume of cell nucleus was
1377 used as a proxy of total cell volume because nuclear volume is known to scale in proportion to
1378 cell volume and the the nucleus can be segmented and measured much more accurately that the
1379 irregular-shaped cell[76].
1380

1381 **siRNA transfection**

1382 For siRNA screening, the library was purchased from Horizon Discovery. We constructed two
1383 customized libraries against the target genes listed in Extended Data Table 1. We used ON-
1384 TARGETplus siRNA (Horizon Discovery), with 4 different siRNA sequences targeting the same
1385 gene pooled together. siRNA transfection was performed using Lipofectamine RNAiMAX
1386 (Invitrogen) following the manufacturer's protocol. Briefly, for reverse transfection, 7500 HMEC
1387 cells with Clover-3xFlag-Rb variant cassettes (15000 cells if the variant is RbΔCDK because the
1388 cells will be arrested in G1) suspended in 100μL doxycycline containing medium (1μg/mL) were
1389 added per well into a 96-well plate containing a mixture of pooled siRNAs (1.5pmol per well) and
1390 Lipofectamine RNAiMAX (0.2μL per well in 20μL OptiMEM). Cells were subsequently grown for
1391 48 hours at 37°C before fixation. For MLN4924, TAK243, and Bortezomib treatments, the drugs
1392 were added 5 hours before fixation. Cells were fixed with 4% paraformaldehyde for 20 minutes at
1393 room temperature, permeabilized with 0.5% Triton™ X-100 (Sigma-Aldrich) for 15 minutes at
1394 room temperature, and then incubated with 500 nM DAPI for 30 minutes at room temperature.
1395 After PBS wash, cells were imaged using the ImageXpress Micro Confocal at the High-
1396 Throughput Screening Knowledge Center of Stanford.

1397 For regular siRNA knockdown, we used the Silencer-Select Pre-designed siRNA (Ambion Thermo
1398 Fisher). For most genes, we purchased 2 different siRNAs. Lipofectamine RNAiMAX (Invitrogen)
1399 was used for siRNA transfection. For 24-well plates, cells were plated 1 day before such that they
1400 were ~40% confluent at the time of transfection. For each well, 6 pmol of siRNA in 50 μl Opti-
1401 MEM was mixed with 1 μl RNAiMAX in 50 μl Opti-MEM. After 10-20 minutes of incubation at room
1402 temperature, the mixture was added to the cells. 48 hours later, the cells were lysed for western
1403 blot or qPCR analysis.

1404 **Palbociclib sensitivity assay**
1405 Cells were plated in 96-well plates (2000/well) 1 day before drug treatment. For cells with inducible
1406 Rb cassettes, cells were plated in different concentrations of doxycycline (0, 20ng/ml, 50ng/ml,
1407 150ng/ml, 500ng/ml, 1000ng/ml) to induce different concentrations of Clover-3xFlag-Rb.
1408 Palbociclib or DMSO were added the next day, and the medium was refreshed every day. After
1409 3 days of drug treatment, cells were fixed with 4% paraformaldehyde for 20 minutes at room
1410 temperature, permeabilized with 0.5% Triton™ X-100 (Sigma-Aldrich) for 15 minutes at room
1411 temperature, and then incubated with 500 nM DAPI for 30 minutes at room temperature before
1412 imaging. After PBS wash, cells were imaged using the ImageXpress Micro Confocal at the High-
1413 Throughput Screening Knowledge Center of Stanford. Cell nuclei were segmented and counted
1414 to indicate cell number. 4 technical replicates were prepared for each condition (4 wells for the
1415 same genotype and same treatment), and the average was used for the final cell count.
1416
1417 **Immunofluorescence staining**
1418 Cells were seeded on a 35-mm glass-bottom dish (MatTek) or a 6/24-well glass-bottom plate
1419 (Cellvis) one day before immunofluorescence staining. For this staining, cells were fixed with 4%
1420 paraformaldehyde for 20 minutes at room temperature, permeabilized with 0.5% Triton X-100
1421 (Sigma-Aldrich) for 15 minutes at room temperature, and then blocked with 3% BSA in PBS. Then,
1422 the cells were incubated with primary antibodies overnight at 4°C. After 3 washes with PBS, the
1423 cells were incubated with Alexa Fluor secondary antibodies (Invitrogen, A32728) at 1:1000 for 1
1424 hour at room temperature. After 3 washes with PBS, cells were incubated with 500 nM DAPI for
1425 30 minutes at room temperature before imaging. The primary antibodies used for
1426 immunofluorescence were Anti-Rb (Santa Cruz, sc-74570, 1:100), Anti-phospho-Rb (S807/811)
1427 (CST, 8516, 1:400). The cells were imaged using a Zeiss Axio Observer Z1 microscope with an
1428 A-plan 10x/0.25NA objective. For the 24-well plates, cells were imaged using the ImageXpress
1429 Micro Confocal from the High-Throughput Screening Knowledge Center at Stanford.
1430

1431 **Flow cytometry and cell sorting**
1432 For flow cytometry analysis, cells were grown on 6-well plates to ~70% confluence and harvested
1433 following trypsinization. The cells were then fixed with 4% formaldehyde for 10 minutes at 37ºC
1434 and permeabilized with 90% ice-cold methanol for 30 minutes on ice. Fixed and permeabilized
1435 cells were washed once with PBS, blocked with 3% BSA in PBS for 30 minutes at 37ºC, and then
1436 stained with primary antibodies for 2 hours at 37ºC. The cells were then washed twice with a wash
1437 buffer (1% BSA in PBS + 0.05% Tween® 20), stained with the fluorophore-conjugated secondary
1438 antibodies (Life Technologies) at 1:1000 dilution for 1 hour at 37ºC, and then washed twice again.
1439 After this treatment, the cells were resuspended in PBS containing 3 μM DAPI for DNA staining,
1440 incubated for 30 minutes at room temperature, and then analyzed on an Attune NxT Flow
1441 Cytometer (Thermo Fisher Scientific). For live cell flow cytometry analysis, cells were harvested
1442 from dishes by trypsinization, stained with 20 μM Hoechst 33342 DNA dye in PBS for 30 minutes
1443 at 37ºC and then analyzed on an Attune NxT Flow Cytometer (Thermo Fisher Scientific). For live
1444 cell sorting, the cells were harvested from dishes following trypsinization, resuspended in fresh
1445 medium, stained with Hoechst (if sorting by cell cycle phase), and then sorted on a BD FACSAria
1446 flow cytometer. DNA content and the mCherry-Geminin fluorescent reporter were used to
1447 determine cell cycle phase, and the side scatter area parameter was used as a readout for cell
1448 size. During sorting, cell samples were kept at 4ºC, and the sorted cells were collected for further
1449 RNA isolation and RT-qPCR analysis or for immunoblotting. For single clone derivation, cells
1450 were sorted into 48-well plates containing growth medium using the single-cell sorting mode.
1451
1452 **RNA immunoprecipitation assay**
1453 We performed RNA immunoprecipitation following published protocols [77]. Briefly, cells were lysed
1454 in an ice cold polysome lysis buffer with 3-5 million cells per 1 ml of lysis buffer. The lysate was
1455 spun down at 16000xg for 15 minutes at 4°C, and the supernatant was transferred to a new tube.
1456 50μl of equilibrated protein A/G-agaraose beads (Pierce, Thermo Fisher) were added to the
1457 supernatant for preclearing at 4°C for 1h. 100μl of the lysate was saved as the input sample, and
1458 the rest was incubated with 5μg of eIF4E antibody (sc-271480, Santa Cruz) or Mouse IgG (sc-
1459 2025, Santa Cruz) at 4°C overnight. The next day, 50μl of equilibrated protein A/G-agaraose
1460 beads were added to each sample and rotated at 4°C for 4 hours. Then, 100μl of the supernatant
1461 was saved for the flow-through sample, and the beads were washed with lysis buffer 2 times, and
1462 then washed with lysis buffer containing 1M urea another 2 times. Then, the beads were boiled
1463 in Tris-EDTA containing 1% SDS and 12% β-Mercaptoethanol before RNA was extracted using
1464 a Direct-zol RNA Microprep kit (Zymo Research). The extracted RNA was then prepared for RT-
1465 qPCR analysis to examine *RB1, Actin*, and *GAPDH* expression.
1466
1467 **Co-immunoprecipitation**
1468 Cells were lysed in lysed in 1% NP-40 lysis buffer (50 mM HEPES, 150 mM NaCl, 1% NP-40, 1
1469 mM EDTA with protease inhibitor mixture and 1 mM PMSF). Lysates were incubated on ice for
1470 30 minutes before clearing by centrifuging at 16,000 × g at 4°C for 20 min. Protein lysates were
1471 pre-cleared with Protein A/G plus agarose beads (SCBT, sc-2003) at 4°C for 1 hour. Then, 8% of
1472 cleared lysates were taken as input, the rest were incubated with either 5 μg FLAG M2 antibody
1473 (Millipore Sigma #F1804) or Mouse IgG control (BioLegend, 400101) on a rotor at 4°C for 2 hours.
1474 Then, Protein A/G plus agarose beads (SCBT, sc-2003) beads were added to each sample,
1475 incubated on a rotor at 4°C for 2 hours. Then, beads were washed in 1% NP-40 lysis buffer 3
1476 times, 10 minutes each time at 4°C on a rotor. The immunoprecipitated proteins were then eluted
1477 in 1x Sample Buffer 2 (Invitrogen, 1981103) by boiling at 95°C for 10 minutes. And then, the
1478 samples were analyzed by immunoblot.
1479
1480 **Immunoblots**

Cells were directly lysed with 1x NuPAGE LDS Sample buffer (Invitrogen), and then incubated at 95°C for 10 minutes. Lysates were separated on NuPAGE 3-8% Tris-Acetate protein gels (Thermo Fisher Scientific), and transferred to nitrocellulose membranes. Membranes were then blocked with SuperBlock™ (TBS) Blocking Buffer (Thermo Fisher Scientific) and incubated overnight at 4°C with primary antibodies in 3% BSA solution in PBS. The primary antibodies were detected using the fluorescently labeled secondary antibodies IRDye® 680LT Goat anti-Mouse IgG (LI-COR 926-68020) and IRDye® 800CW Goat anti-Rabbit IgG (LI-COR 926-32211). Membranes were imaged on a LI-COR Odyssey CLx and analyzed with LI-COR Image Studio software. The following primary antibodies were used: anti-β-Actin (Sigma, A2103, 1:2000), anti-Rb (Santa Cruz, sc-74570, 1:500), anti-UBR5 (ABE2863, Millipore, 1:2000), anti-Tubulin (T5168, Sigma, 1:2000), and anti-GAPDH (AB2302, Sigma, 1:2000).

Image analysis

For live-cell imaging microscopy data, cell nuclei were segmented using the GFP channel from either the endogenously expressed Rb-3xFLAG-Clover-sfGFP or the inducibly overexpressed Clover-3xFlag-Rb variants. For fixed cell imaging microscopy data, cell nuclei were segmented using the DAPI DNA staining signal. Segmentation was performed using the Fiji plugin StarDist, which is a deep-learning tool for segmenting nuclei in images that are difficult to segment using thresholding-based methods. The total pixel intensities within the segmented masks in each channel were recorded, and each object's background was subtracted based on the median intensity of the image. Nuclear volume was used as a proxy for cell size, and calculated as the nuclear area$^{3/2}$. The tracking of live cells was done manually using the TrackMate plugin in Fiji. To determine the protein half-life, the degradation traces were fitted with an exponential decay function $N = N_0\exp(-kt)$ so that the half-life $t_{1/2} = (1/k)(\ln 2)$.

RNA extraction and RT-qPCR

Total RNA was isolated using a Direct-zol RNA Miniprep kit (Zymo Research). For RT-qPCR, cDNA synthesis was performed with 1µg of total RNA using an iScript Reverse Transcription Kit (Biorad). qPCR reactions were made with the 2x SYBR Green Master Mix (Biorad). Gene expression levels were measured using the ΔΔCt method.

Mathematical Model of Rb concentration dynamics

The mathematical model of Rb dynamics consists of two main equations. The first describes the time evolution of cell mass as $\frac{dM}{dt} = \gamma M^{\delta}$, where M denotes the cell mass, δ<1 quantifies the departure from pure exponential growth as measured in [78], and γ is a constant. The second equation describes the evolution of the amount of Rb in the cell as $\frac{dRb}{dt} = \alpha M^{\delta} - \beta(t)\, Rb$, where α is an effective synthesis rate and $\beta(t)$ is a time-varying degradation rate. Therefore, the amount of Rb synthesized at a given time is proportional to the cell's growth rate. The distinctive element in this model is the time-dependence of the degradation rate $\beta(t)$, which reflects the cell-cycle-dependent changes in Rb stability. It is encoded as a step change such that $\beta(t) = \beta_0$ as long as the cell is in G1 phase and that $\beta(t) = \varepsilon\beta_0, \varepsilon < 1$, when the cell is in S/G2/M phase. To compare the relative contributions of cell-cycle-dependent synthesis and degradation changes, we also consider the case where β is a constant and α increases slightly in a step change at the G1/S transition. The cell goes through the G1/S transition when the concentration of Rb in the cell crosses a threshold value set *a priori*. The S/G2/M phase is represented as a timer in the model. The model is integrated in time with an Euler forward method. From arbitrary initial conditions, the model is run through a "burn-in" period until it reaches a limit cycle described by the input parameters. The model is available on GitHub (https://github.com/LucasFuentesValenzuela/RB_model).

Genomic analysis of breast cancer patients

We extracted the copy number data from Pereira et al., Nat. Commun 2016 [79] (ASCAT) and we used the IC subtypes reported in the Rueda et al. Nature 2019 study [58]. We performed survival analysis using Cox's proportional hazard models using R package survival (version 3.5-7) and corrected for key clinical covariates as described in [58] (*e.g.*, age, grade, tumor size, lymph node, and ER status). We generated Kaplan–Meier and forest plots using the R package survminer (version 0.4.9).

Statistical analysis

The data in most Fig. panels reflect multiple biological replicate experiments performed on different days. The mouse experiments used mice derived from different litters. For comparison between groups, we generally conducted unpaired two-tailed Student's t-tests. Statistical significance is displayed as $p < 0.05$ (∗) or $p < 0.01$ (∗∗) unless specified otherwise.